


**Special Collection:**

Years of the Maritime Continent

**Key Points:**

- Two wet cold surges produced locally extreme rainfall over Singapore in January 2021 and were followed by two dry surges
- The dynamics of the January 2021 cold surges and the associated convection are explored in convection-permitting forecasts
- The combination of the cold surge and a tropical low produced strong, moist north-easterlies, and heavy rainfall over the Singapore region

**Correspondence to:**

I. Tan,  
isaac.tan@monash.edu

**Citation:**

Tan, I., Reeder, M. J., Birch, C. E., Peatman, S. C., & Webster, S. (2024). Synoptic and mesoscale dynamics of cold surges over the South China Sea and their control on extreme rainfall. *Journal of Geophysical Research: Atmospheres*, 129, e2024JD040822. <https://doi.org/10.1029/2024JD040822>

Received 21 JAN 2024  
Accepted 27 JUL 2024

## Synoptic and Mesoscale Dynamics of Cold Surges Over the South China Sea and Their Control on Extreme Rainfall

I. Tan<sup>1</sup> , M. J. Reeder<sup>1,2</sup> , C. E. Birch<sup>3</sup> , S. C. Peatman<sup>3</sup> , and S. Webster<sup>4</sup>

<sup>1</sup>School of Earth, Atmosphere and Environment, Monash University, Clayton, VIC, Australia, <sup>2</sup>Australian Research Council Centre for Climate Extremes, Sydney, NSW, Australia, <sup>3</sup>Institute of Climate and Atmospheric Science, School of Earth and Environment, University of Leeds, Leeds, UK, <sup>4</sup>UK Met Office, Exeter, UK

**Abstract** We investigate the synoptic and mesoscale dynamics of two wet and two dry cold surges in January 2021 using a combination of observations, reanalysis, and convective-scale model forecasts from the Met Office Unified Model (MetUM). We focus on the wet surges, and particularly the wettest days which are locally extreme over Singapore and the surrounding region (i.e., the daily mean and area-averaged rainfall over 20 years exceeds the 99th percentile). On the large scale, the wet surges are characterized by an anomalously strong anticyclone over Siberia prior to their onset. The anticyclone and resultant surge winds are stronger than those of the dry surges. There is also a relatively moist (dry) environment prior to the onset of the wet (dry) surges, with the Madden-Julian Oscillation (MJO) being in Phase 3 (Phase 6). On the mesoscale, the combination of the cold surge and a local tropical low produce strong, moist north-easterly winds and convection over the Singapore region. The equatorward advection of positive anomalies of equivalent potential temperature resembles a weak gravity-current-like structure at its head, although the spatial scale is much too large for a gravity current. There is a moist bias in the model forecasts, although the precipitation is underestimated regionally during the wet surges and particularly on the extreme rainfall days. Overall, the model forecasts perform well synoptically but not in the details of mesoscale convection.

**Plain Language Summary** Cold surges are weather systems in the winter monsoon that bring strong north-easterly winds, colder air, and sometimes very heavy rainfall and flooding to Singapore and the surrounding region. We investigate the structure and development of two wet and two dry cold surges in January 2021 using a combination of observations and high-resolution model forecasts. We focus on the wet surges, and especially the wettest days, which are characterized by very heavy rainfall over Singapore and the surrounding region. The wet surges are driven by a very strong high-pressure system over Siberia, which results in strong north-easterly winds. These north-easterlies are stronger in the wet surges than in the dry surges. A relatively moist (dry) environment precedes the wet (dry) surges. On the smaller scale, the combination of the cold surge and a local tropical low-pressure system produce strong, moist north-easterly winds and heavy rainfall over the Singapore region. Overall, the model forecasts the large-scale well but not the smaller-scale details of heavy rainfall.

### 1. Introduction

Cold surges are synoptic weather systems found over the South China Sea during the boreal winter (November–March; NDJFM). They are characterized by the strengthening of prevailing low-level northerly to north-easterly winds, temperature falls of a few degrees over several days, and in some cases, heavy prolonged rainfall and flooding (e.g., Chang et al., 1979, 2004, 2005; Ding, 1994; Fong & Ng, 2012; Johnson & Chang, 2007; Lim et al., 2017; MSS, 2023; Pullen et al., 2015; Ramage, 1971; Tan et al., 2023; Tangang et al., 2008; Wu et al., 2007; Xavier et al., 2020). Heavy rainfall associated with cold surges affect the equatorial coastal regions of Southeast Asia such as Vietnam, the Malaysian Peninsula, and Singapore, particularly between November and January (Fong & Ng, 2012; MSS, 2023). According to the 2021 climatological report by the Meteorological Service Singapore (MSS, 2022), two consecutive surges on 1–2 January and 8–13 January were responsible for the second wettest January on record over Singapore since rainfall records began in 1869. In the first fortnight alone, 648.4 mm was recorded over the Singapore climate station at Changi, which was highest in the last 30 years. The highest daily totals for the two surges were 210.6 and 204.0 mm on 2 and 10 January, respectively. The Changi climate station also recorded a monthly mean temperature of 26.0°C, which was the lowest for January in the last

© 2024, The Author(s).

This is an open access article under the terms of the Creative Commons Attribution License, which permits use, distribution and reproduction in any medium, provided the original work is properly cited.

30 years. Over the Malaysian Peninsula, the surges resulted in major flooding, at least 6 deaths, and close to 50,000 individuals evacuated (News.Az, 2021; OCHA Services, 2021).

On the large scale, the wet surges followed two record-breaking cold air outbreaks over China, the first from 29 December 2020–1 January 2021, and the second from 6–8 January 2021 (Zheng et al., 2022). These outbreaks and surges were driven by the strengthening of the Siberian high, which dominates the low-level circulation over Asia during the boreal winter (e.g., Ding, 1994; Fong & Ng, 2012; Hongming et al., 2022; Lau & Li, 1984; Lim & Chang, 1981; Zhang et al., 2022; Zheng et al., 2022). The Siberian high was particularly strong, peaking close to 1,050 hPa, which is about 20 hPa above the 1981–2010 climatology (see Figure 5c of Zhang et al., 2022). The southward intrusions of the Siberian high resulted in sudden surges of strong northerly to north-easterly winds that propagated toward China and the South China Sea, leading to the wet and cool conditions over Southeast Asia. According to Lim and Chang (1981), these surges can be interpreted as linear wave responses to the Siberian high, where the northerly winds turn to become north-easterly as the Rossby wave group is established. Hai et al. (2017) also showed that the strong Siberian high and north-easterly surge winds were connected to heavy rainfall and severe flooding over the East Coast of the Malaysian Peninsula in November and December 2014. They found that the strong surge winds resulted in a strong cyclonic shear to the north of the near-equatorial trough, which was necessary for the development and maintenance of deep convection over the region.

The Siberian high is not the only meteorological factor during such record-breaking cold surges. According to Kumar (2021) and Kumar et al. (2019), there are linkages between the Siberian high, extratropical cyclones in the North Pacific, and the jet stream over East Asia. The jet stream intensifies the extratropical cyclones, while a stronger Siberian high and the consequent larger pressure differences between it and these cyclones intensify and prolong the cold surges. Moreover, Xia et al. (2024) found that 92% of all cold surges are accompanied by these cyclones, which advect cold air masses from the high-to mid-latitudes, widening the thermal contrast between the mid- and low-latitudes, and thereby strengthening and sustaining cold surges that affect the South China Sea. Zhang et al. (2022) and Hongming et al. (2022) have also suggested that the exceptionally strong cold air outbreak and cold surges in January 2021 were due to a major sudden stratospheric warming. Hongming et al. (2022) found that there was a rise in the stratospheric temperature of more than 40°C at the beginning of January 2021, which according to Zhang et al. (2022), displaced the stratospheric polar vortex toward East Asia, shifted the tropospheric polar vortex off the pole toward East Asia, and strengthened a blocking anticyclone over the Ural-Siberia region. The stronger Siberian high and Ural blocking resulted in record-breaking cold anomalies of approximately –10°C over China or East Asia (see Figure 1 of Hongming et al., 2022). Moreover, Ma et al. (2022) connected the strong cold surges over East Asia to increased tropical convection over the western tropical Pacific (which includes the Maritime Continent region) about 6–8 days after the surge onset.

In contrast to the exceptionally wet conditions during the first fortnight of January 2021, the second half of January was warmer and drier, with a total rainfall of 44.2 mm over Changi (MSS, 2021). Based on the climatological report, the drier conditions continued into February as the dry phase of the north-east monsoon conditions over Singapore and the surrounding region was associated with the southward movement and narrowing of the Intertropical Convergence Zone (ITCZ; McBride et al., 2015; MSS, 2022; Xavier et al., 2020). Consequently, February 2021 was the second driest on record with only 1.0 mm of rainfall recorded at Changi. According to Hongming et al. (2022) there was an abrupt transition from the cold period from 21 November 2020–11 January 2021, to the warm period from 19 January–28 February 2021. This abrupt transition was also attributed to the effect of stratospheric warming on the troposphere.

The above studies have provided some insight into the synoptic aspects of the cold surges in January 2021, particularly their connection to the cold air outbreaks over East Asia and the strong Siberian high. The record-breaking surges in the first half of the month were driven by synoptic processes at the high-to mid-latitudes that forced smaller-scale convective structures over the equatorial South China Sea. However, the mechanisms by which the resultant convection and extreme rainfall develop on the mesoscale are not well understood. These mechanisms are presumably better represented in convection-permitting models. According to Clark et al. (2016), convection-permitting models are run at resolutions high enough to eliminate the need for convective parameterizations and are used operationally to forecast precipitation over many parts of the world. In the case of cold surges and their associated convection, it is unclear how well the mesoscale propagation is represented over the equatorial South China Sea because of the complex topography and intricate configuration of islands in this region (Argüeso et al., 2020; Neale & Slingo, 2003).

The Met Office Unified Model (MetUM) is a numerical weather prediction (NWP) model that is run routinely at convection-permitting resolutions (Davies et al., 2005). Lean et al. (2008) showed that running the MetUM at convection-permitting grid spacing's of 4 and 1 km produced more realistic precipitation fields than the equivalent runs with 12 km grid spacing and parameterized convection. Similar results were found in more recent studies by Dipankar et al. (2020), Ferrett et al. (2021), and Senior et al. (2023), who evaluated the high-resolution forecasts over Southeast Asia. Of particular interest to the current work is the study by Dipankar et al. (2020) who demonstrated the benefits of convection-permitting simulations over Singapore and the surrounding region compared to parameterized simulations. They used the SINGV model, which is a modification of the limited-area convection-permitting version of the MetUM with a domain covering Singapore, the Malaysian Peninsula, and Sumatra. SINGV compared well with the observations, including the squall lines that often affect Singapore, and was much better than the global parameterized model that uses the Global Atmosphere 6.1 (GA6.1) configuration. Senior et al. (2023) evaluated the development of convectively-coupled Kelvin waves (CCKWs), which are eastward traveling tropical weather systems that organize convection and form an important mode of equatorial rainfall variability over the Maritime Continent (Ferrett et al., 2020; Senior et al., 2023; van der Lin et al., 2016). They found that the development of CCKWs over the Indian Ocean was better represented in the MetUM South East Asia (SEA) convection-permitting limited area models than the global parameterized model. Ferrett et al. (2021) evaluated the precipitation forecast on three domains, covering Malaysia, Indonesia, and the Philippines. Although the model forecast skill decreased with lead time, the skill varied depending on the time of day, particularly over Malaysia and Indonesia since the rainfall is more spatially constrained by orographic features when over land. It was found that the skill was highest during the daytime when the precipitation is predominantly over the land and fixed to the orography, and lowest at night when the precipitation is offshore.

Of particular relevance to cold surges is the study by Xavier et al. (2020) who evaluated the performance of the MetUM in simulating the seasonal cycle, the interactions between cold surges and cross-equatorial surges, and the Madden Julian Oscillation (MJO). They utilized two climate configurations of the MetUM, namely the Global Coupled configuration 3.0 (GC3.0) and Global Atmosphere 7.0 (GA7.0), in both of which the convection is parameterized. While the seasonal cycle of cold surges was captured reasonably well, both climate models tended to generate more cold surges and cross-equatorial surges in February compared to observations, while the GA7.0 model produced fewer surges in December. The GA7.0 model simulations show a dry bias over most of the western Maritime Continent region, while a mix of relatively smaller wet and dry biases are evident in the GC3.0 model. To date, cold surges and their associated convection have been evaluated in the coarser resolution models with parameterized convection, but not in the high-resolution convection-permitting models.

In this paper, we use the high-resolution convection-permitting MetUM forecasts to analyze and evaluate the structure and development of wet and dry cold surges using specific case studies in January 2021 on both the synoptic and mesoscales. The aims of the work are to (a) better understand the response of convection to cold surges at the synoptic and mesoscales; (b) evaluate the ability of a convection-permitting model to forecast them. We particularly focus on the two wet cold surges that affected Singapore and the surrounding region in the first half of January 2021. Section 2 outlines the data used, and Section 3 provides an overview of the wet and dry cold surges in January 2021 from the perspective of extreme rainfall in the observations and reanalysis. Section 4 describes the synoptic of the two wet surges in January 2021 using the reanalysis data. Section 5 evaluates the MetUM forecasts against the reanalysis and observational data sets both spatially and temporally. Section 6 specifically investigates the mesoscale aspects of the first wet surge and the associated convection using the model forecasts. Conclusions follow in Section 7.

## 2. Data: MetUM Forecasts, Reanalysis, and Observations

In this study with the MetUM, we use real-time single member convective-scale forecasts at 4.4 km horizontal grid spacing. These simulations are a regional downscaling of global analysis fields, meaning that no data assimilation is used. In other words, the model is initialized from the global analysis using the cold-start mode (Short & Petch, 2022; Warner et al., 2023). The domain covers approximately 18°S–30°N, 90°E–154°E. Our study uses the 0800 LST forecast runs at 3-hourly intervals at the lead times from 12 to 33 hr (to allow for model spin-up) between 25 December 2020 and 10 February 2021. In the vertical, 16 pressure levels between 1,000 hPa and 100 hPa (excluding surface data) have been archived for analysis. The following MetUM fields are used in this study: total column water vapor (TCWV), zonal and meridional winds, vertical wind (W), temperature, relative humidity, and the hourly-averaged precipitation rate (at 3-hourly intervals for consistency with the other

**Table 1**  
*Changes in the RAL Version Package in the MetUM Forecasts*

Year	RAL version package	Purpose
2017–2018	Prototype of RAL1-T	Improved representation of turbulence and cloud scheme. There are three extra prognostic fields, namely liquid fraction, ice fraction, and mixed-phase fraction (Bush et al., 2020).
2018–2019	Shift from RAL1-T to RAL2-T	Added reduced drag at high wind speeds in RAL1-T. The shift to RAL2-T improved the intensity of tropical cyclones (Bush et al., 2022; Togerson et al., 2023).
October 2019 onwards	RALs2-T	RAL2-T package fully implemented, and outperforms RAL1-T in the Southeast Asia region by significantly improving precipitation forecasts for times between 24 and 72 hr (Bush et al., 2022)

fields). Anomalies of various diagnostics are computed by subtracting the daily mean climatology of the model forecasts at the same lead times over a 5-year period from DJF 2017–2018 to 2021–2022. Precipitation anomalies are not part of the analysis as the climatology is very noisy.

There have also been several updates to the Regional Atmosphere and Land (RAL) science configurations for kilometer-scale forecasting in the MetUM. These updates were implemented in the change from RAL version 1.0 Tropical (RAL1-T; Bush et al., 2020) to version 2.0 (RAL2-T; Bush et al., 2022) from October 2019 onwards as described in Table 1 below. Both RAL1-T and RAL2-T define the science configurations of the dynamics and physics schemes of the atmosphere and land. The cold surge case studies in January 2021 occur after the RAL2-T package has been fully implemented, although the climatology combines forecasts using both the RAL1-T (DJF 2017–2018 to 2018–2019) and RAL2-T (DJF 2019–2020 to 2021–2022) configurations.

We use the definition of cold surges from Tan et al. (2023) which is based on the NDJFM 2000–2001 to 2019–2020 observed climatology where:

1. The mean sea-level pressure (MSLP) exceeds 1,020 hPa anywhere within the region from 18 to 22°N, and 105 to 122°E (brown box in Figure 1).
2. The horizontal wind speed at 925 hPa is at least 0.75 standard deviations above the climatological mean when averaged over the region from 5 to 10°N, and 107 to 115°E (magenta box in Figure 1).
3. The wind direction at 925 hPa over the same region is between 337.5° and 90°.

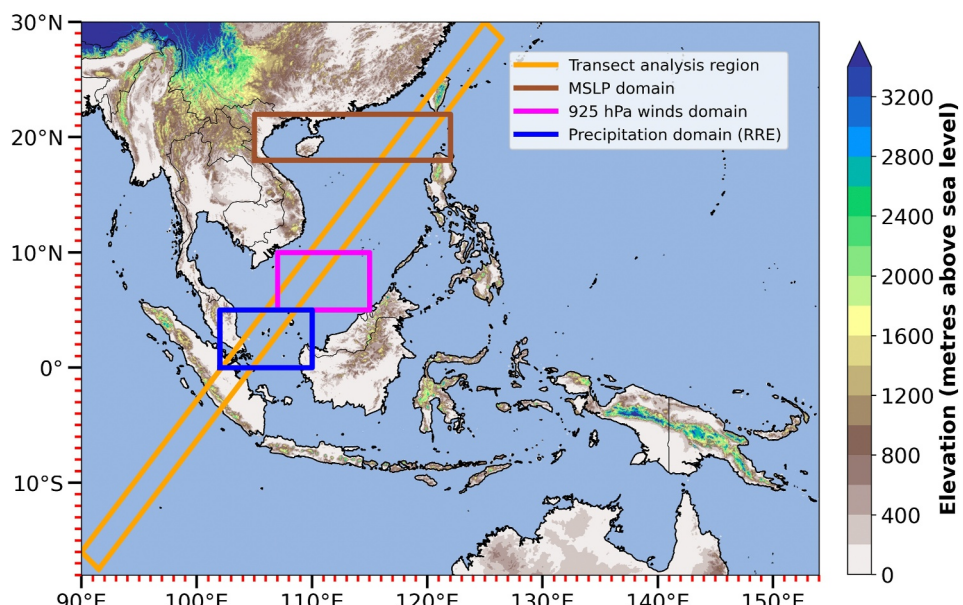


**Figure 1.** Map covering the entire model forecast domain that depicts the transect analysis region (orange box), the cold surge indices domains for MSLP (brown box) and horizontal winds at 925 hPa (magenta box), and the precipitation domain that is used to define wet and dry cold surges (blue box). Adapted from Figure 1 of Tan et al. (2023).

4. The above three conditions are satisfied for at least two consecutive days (Ding, 1990).

Tan et al. (2023) defined wet and dry cold surges by the upper and lower precipitation quartiles over the same climatological period. The thresholds for each category (approximately  $17.4 \text{ mm d}^{-1}$  for wet surges and  $3.5 \text{ mm d}^{-1}$  for dry surges) were based on the average precipitation over a domain encompassing Singapore and parts of Malaysia, Sumatra, and Borneo ( $0\text{--}5^\circ\text{N}$ ,  $102\text{--}110^\circ\text{E}$ ; blue box in Figure 1).

The MetUM forecasts are evaluated against the fifth reanalysis of the European Center for Medium-Range Weather Forecasts (ECMWF ERA5; Hersbach et al., 2020) and Global Precipitation Measurement (GPM; Huffman et al., 2019) rainfall data. For GPM, the multi-satellite precipitation estimate with gauge calibration field (i.e., “precipitationCal”) is used within the data set that contains the final estimate of precipitation (i.e., GPM IMERG Final Precipitation L3). We evaluate the forecasts at 3-hourly temporal resolution for consistency. Here, the MetUM forecasts are re-gridded to the horizontal grid spacing of ERA5 ( $0.25^\circ \times 0.25^\circ$ ) except for rainfall which is re-gridded to the grid spacing of GPM ( $0.1^\circ \times 0.1^\circ$ ). Anomalies for the ERA5 reanalysis are calculated using the same 5-year climatological period as the MetUM forecasts. Where no comparisons with the model forecasts are made, hourly resolution is used (daily accumulated precipitation for GPM) and anomalies are taken relative to the DJF 2000–2001 to 2019–2020 observed climatology.

Following Tan et al. (2023), we also take the average over 7 transects aligned from south-west to north-east along the South China Sea that are spaced at  $0.25^\circ$  intervals (orange box in Figure 1). The horizontal grid spacing of interpolation along each transect (nearest-neighbor method) follows the grid spacing of the respective data set used.

### 3. Extreme Rainfall and Cold Surges in January 2021

#### 3.1. Climatology of Extreme Rainfall

This section places the extreme rainfall associated with the two strong cold surges within the first half of January 2021 in a broader climatological context. We define an extreme rainfall day relative to the NDJFM 2000–2001 to 2019–2020 climatology in two ways:

1. The mean rainfall over the precipitation domain (blue box in Figure 1) on a given day exceeds the 99th percentile (31 extreme rainfall days, 22 of which are surge days). The extreme wet threshold is approximately  $43.0 \text{ mm d}^{-1}$  based on the daily accumulated GPM data. Rainfall extremes satisfying this definition will be termed Regional Rainfall Extremes (RRE).
2. The mean rainfall over a smaller box over Singapore ( $1.0\text{--}1.5^\circ\text{N}$ ,  $103.5\text{--}104.5^\circ\text{E}$ ) within the RRE on a given day exceeds the 99th percentile (31 extreme rainfall days, 17 of which are surge days). The extreme wet threshold is approximately  $66.0 \text{ mm d}^{-1}$  based on the daily accumulated GPM data. Rainfall extremes of this type will be called Singapore Rainfall Extremes (SRE).

The 20-year period here follows the climatology used in Tan et al. (2023) given that a large number of days is required to reliably determine extreme rainfall days based on percentiles.

To better understand the climatology of extreme rainfall, we analyze the relationship between rainfall and the mid-tropospheric buoyancy in an idealized entraining plume. We follow the formulation of Adames et al. (2021) and calculate the plume buoyancy ( $B_L$ ). The analysis is similar to Tan et al. (2023) who applied these ideas to a study of the local thermodynamics of convection associated with cold surges in the region. We composite the extreme rainfall days for both the RRE (Figures 2a and 2b) and SRE definitions (Figures 2c and 2d). Following Tan et al. (2023), composite maps of  $B_L$  are plotted on the domain  $15^\circ\text{S}\text{--}25^\circ\text{N}$ ,  $95^\circ\text{E}\text{--}125^\circ\text{E}$ . According to Adames et al. (2021) and Tan et al. (2023), this precipitation-buoyancy relationship appears to better represent the underlying physical process of tropical moist convection compared to more standard diagnostics such as convective available potential energy (CAPE) and convective inhibition (CIN).  $B_L$  is defined in terms of equivalent potential temperature ( $\theta_e$ ), which is approximately conserved during moist adiabatic processes. Adames et al. (2021) interpret  $B_L$  as a measure of the buoyancy of an air parcel as it rises to the top of the lower free troposphere layer (850–600 hPa), mixing with its environment. Therefore,  $B_L$  is a measure of convective instability of the lower troposphere that accounts for the effects of mixing. As  $B_L$  increases from negative values toward zero, the precipitation increases exponentially (see Figure 3 of Adames et al. (2021)). Moreover, a critical value of  $-0.02 \text{ m s}^{-2}$  marks the beginning of a regime wherein the precipitation increases linearly and rapidly

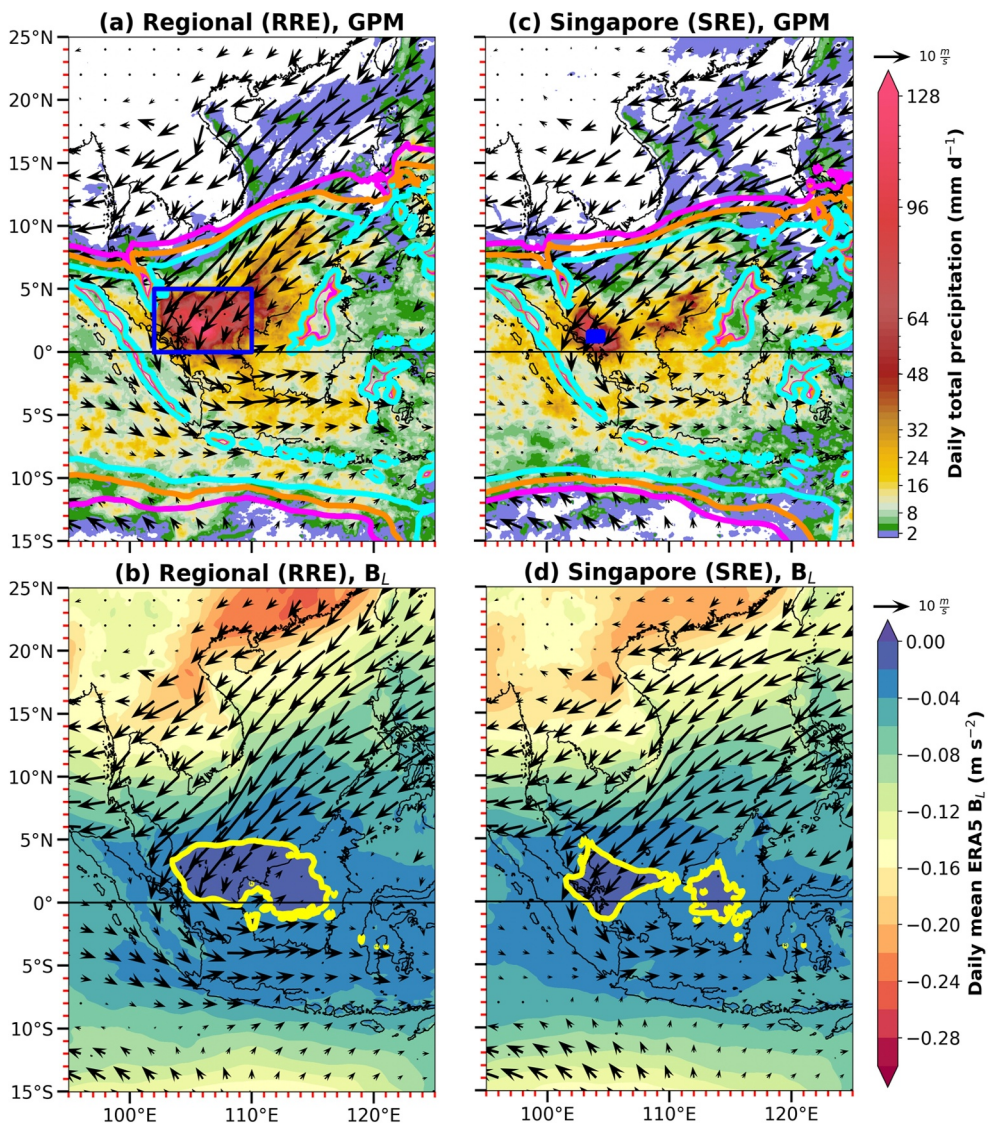


**Figure 2.** Composite means of (a, c) daily total GPM precipitation and (b, d) layer average (850–600 hPa) values of ERA5  $B_L$  for the extreme rainfall composites based on the NDJFM 2000–2001 to 2019–2020 climatology over the domain from 15°S to 25°N, 95°E–125°E. RRE (left column) and SRE (right column) definitions. Daily mean ERA5 925 hPa horizontal wind vectors. The RRE and SRE domains are depicted by the blue boxes in panels (a) and (c), respectively. Magenta, orange, and cyan contours of TCWV are drawn at 46, 48, and 50 mm respectively. The yellow contours are drawn where  $B_L$  is  $-0.02 \text{ m s}^{-2}$ .

with increasing values of  $B_L$ . There is a clear relationship between the regions of extreme rainfall (peaking over 150 mm in the RRE definition and over 120 mm in the SRE definition) and  $B_L$  exceeding  $-0.02 \text{ m s}^{-2}$ . These regions are more widespread in the RRE definition and are associated with north-easterly surge anomalies that span the entire width of the South China Sea. Consistent with findings from Tan et al. (2023), this relationship suggests that these extreme rainfall days are characterized by a moister free troposphere that allows convection to penetrate through the lower troposphere.

For both the RRE and SRE definitions, a vortex is evident in the composite wind off the north-west coast of Borneo, which is often called the Borneo Vortex (e.g., Chang et al., 1979, 2003, 2005; Johnson & Houze, 1987). The surge over the northern South China Sea is also characterized by relatively dry conditions and low values of  $B_L$  (reaching close to  $-0.26 \text{ m s}^{-2}$  in the RRE definition; Figure 2b), resulting in a meridional moisture gradient.

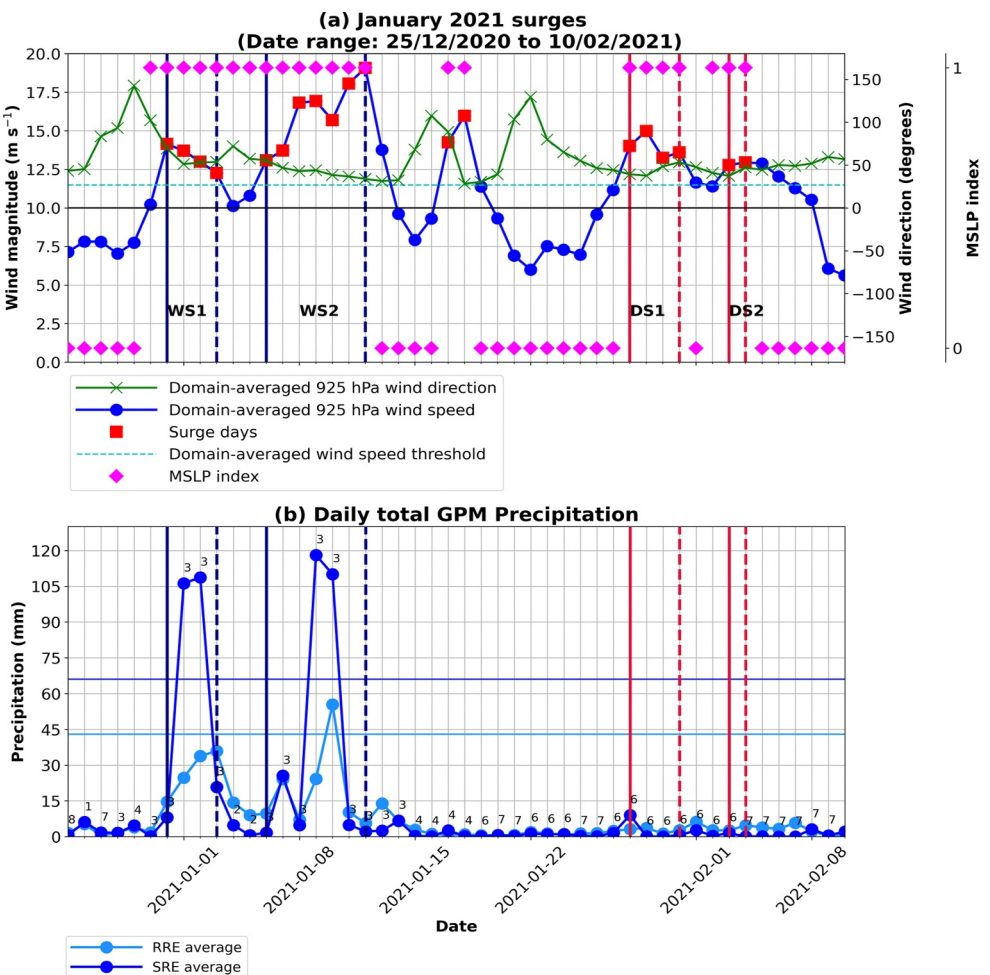


**Figure 3.** (a) Timeseries of cold surge days from 25 December 2020–10 February 2021 based on the Tan et al. (2023) criteria for daily wind speed and direction and MSLP. (b) Timeseries of daily total GPM precipitation for the same period averaged over the RRE (blue) and SRE (light blue) domains. The horizontal lines indicate the rainfall values at the 99th percentile threshold. The MJO phase values are given for each day in panel (b). The solid vertical lines indicate the days of surge onset for WS1 and WS2 (navy lines), and DS1 and DS2 (red lines). The dashed vertical lines indicate the end of each surge period.

Moreover, the 48 mm TCWV contour in both definitions approximately encloses the region over the Tropical Ocean in which convection is found, which is consistent with the moist regime defined by Mapes et al. (2018).

### 3.2. Cold Surges in January 2021 and Extreme Rainfall

We now examine the cold surge case studies in January 2021 from the perspective of wet and dry cold surges. Based on the Tan et al. (2023) definition, there are two wet cold surges from 31 December 2020–3 January 2021 and 6–12 January 2021, which we denote WS1 and WS2 respectively (Figure 3a). WS1 and WS2 cover all the surge dates reported in the 2021 climatological report (MSS, 2022), except for 13 January. When averaged over the RRE domain, the mean precipitation for all days in WS1 and WS2 is approximately  $26.7 \text{ mm d}^{-1}$  and  $19.2 \text{ mm d}^{-1}$  respectively. According to Tan et al. (2023), these amounts exceed the upper quartile and hence, fall within the wet surge category. The next two cold surges from 17 to 18 January and 28 to 31 January 2021 fall within the dry surge category (below the lower quartile). The mean precipitation associated with these dry surges are approximately  $0.8 \text{ mm d}^{-1}$  and  $2.9 \text{ mm d}^{-1}$  respectively over the RRE domain. In the final surge from 3 to 4 February 2021, the mean precipitation is approximately  $3.9 \text{ mm d}^{-1}$ , which is only  $0.4 \text{ mm d}^{-1}$  above the dry surge threshold. We denote the dry surges from 28 to 31 January and 3 to 4 February 2021 as DS1 and DS2, respectively. For brevity, the dry surge days on 17 and 18 January are not analyzed in detail here since this is a

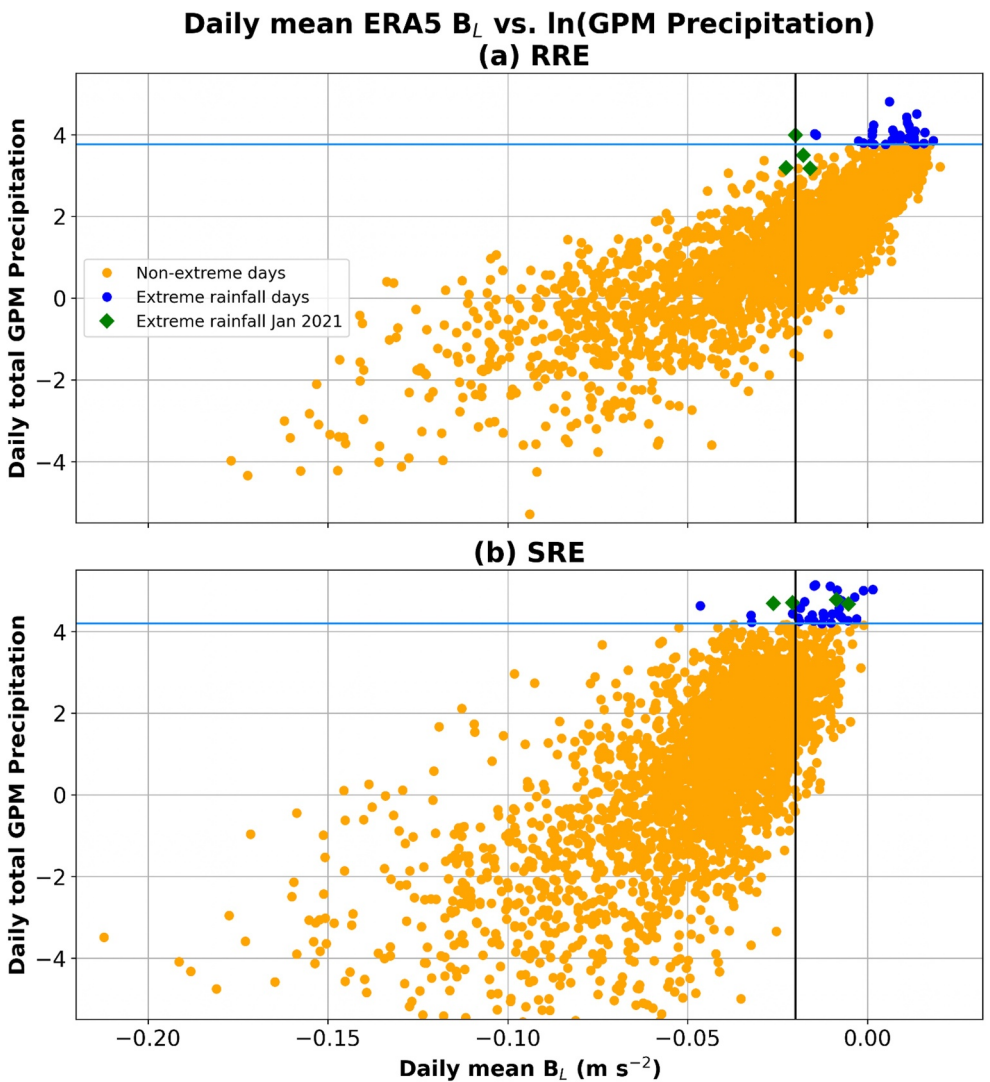


**Figure 4.** Daily total GPM precipitation (natural log taken where the precipitation is exponential in  $\text{mm d}^{-1}$ ) versus daily mean  $B_L$  averaged over the (a) RRE and (b) SRE domains in NDJFM 2000–2001 to 2019–2020. The extreme rainfall days for each definition are marked in blue. Green diamonds represent the four locally extreme rainfall days on 1, 2, 9, and 10 January 2021 based on the SRE definition. The vertical black line is drawn at the  $-0.02 \text{ m s}^{-2}$  boundary for  $B_L$ . The horizontal light blue line is drawn at the natural log of the 99th percentile GPM precipitation value.

short and isolated surge. Moreover, surges with precipitation amounts between the upper and lower quartiles are classified as moderate surges.

There is also a strong relationship between the wet and dry cold surges and the MJO (e.g., Chang et al., 2005; Lim et al., 2017; Tan et al., 2023; Xavier et al., 2020), which is one of the large-scale organizing structures in the tropical atmosphere. The real-time multivariate MJO index (RMM; Wheeler & Hendon, 2004) is used to identify the amplitudes and phases of the MJO. Over the RRE domain, phases 2–3 (phases 5–7) are considered the active (suppressed) phases of the MJO. Days with RMM amplitudes greater than (less than) 1 are considered to be high amplitude (low amplitude) MJO days. For each of the wet surge days, the MJO is consistently in Phase 3 (see MJO phase values in Figure 3b), although the amplitude is less than 1 in WS1 and greater than 1 in WS2. All days in the dry surges are in Phase 6 of the MJO, except for 4 February 2021 which is in Phase 7. The amplitude is greater than 1 for all days in DS1 and DS2.

There is only one RRE day on 10 January 2021, where the daily total rainfall averaged over the domain is 54.1 mm (Figures 3b and 4a). This is the only day within the analysis period that exceeds the threshold of  $43.0 \text{ mm d}^{-1}$ . In

**Table 2***Summary of Synoptic Events Concerning WS1 and WS2*

Dates (Day relative to surge onset)	Synoptic events of importance to WS1 and WS2
28 December 2020 (Day -3, WS1)	Siberian high reaches its peak strength. Positive TCWV anomalies are strongest to the north of the Philippines and south of Taiwan.
30 December 2020 (Day -1, WS1)	Southward intrusion of the Siberian high. Low-pressure system to the east deepens. Meridional TCWV gradient is established.
31 December 2020 (Day 0, WS1)	Surge onset for WS1. Low-pressure system to the east deepens but retreats eastward.
1 January 2021 (Day +1, WS1)	First observed extreme rainfall day.
2 January 2021 (Day +2, WS1)	Second observed extreme rainfall day.
3 January 2021 (Day +3, WS1/Day -3, WS2)	Siberian high reaches peak strength again. TCWV gradient weakens. Low-pressure system to the east weakens and retreats eastward.
5 January 2021 (Day -1, WS2)	Gradual southward intrusion of the Siberian high. Moist environment associated with active MJO in Phase 2 where the RMM amplitude >1 (see Figure 3b).
6 January 2021 (Day 0, WS2)	Surge onset for WS2, MJO in Phase 3 and the RMM amplitude >1.
7–8 January 2021 (Day +1 to Day +2, WS2)	Continued southward intrusion and weakening of the Siberian high. Low-pressure system to the east and the meridional TCWV gradient develop again (not shown in figure).
9 January 2021 (Day +3, WS2)	Further southward propagation and weakening of the Siberian high. Low-pressure system to the east weakens. Meridional TCWV gradient is established. Third observed extreme rainfall day.
10 January 2021 (Day +4, WS2)	Fourth observed extreme rainfall day.
12 January 2021 (Day +6, WS2)	Final day of WS2.

contrast, there are four SRE days on 1, 2, 9, and 10 January (106.2, 108.7, 118.0, and 110.1 mm respectively; Figure 3b). This result suggests that the rainfall here is locally extreme over Singapore but not the larger region, and that intense convective activity associated with these wet surges is highly localized. According to Figure 4b, these four extreme rainfall days fall within the top 10 wettest days of the 20-year climatological period. Over the RRE domain, the precipitation on the four SRE days is also relatively high for the  $B_L$  values (i.e., green diamonds to the left of the  $B_L$  curve in Figure 4a), which suggests that the convection is more efficient than average on those specific surge days. Moreover, there is a weaker precipitation-buoyancy relationship between the daily mean values of  $B_L$  and the natural log of GPM precipitation when averaged over the SRE domain (Pearson correlation coefficient ( $r$ ) = 0.69) compared to the RRE domain ( $r$  = 0.81). Given that Adames et al. (2021) studied the relationship between precipitation and  $B_L$  by averaging over most of the tropics between 15°S and 15°N, one can infer that this relationship does not hold as strongly over a local area compared to the larger scale.

#### 4. Synoptic Description of WS1 and WS2

To better understand the significance of WS1 and WS2, we analyze the synoptic development of the surge and its origin, the Siberian high, using MSLP and 10-m wind anomalies from ERA5. TCWV anomalies are also used to investigate the source of moist air in the wet surges. Table 2 is a chronology of the synoptic events of importance to WS1 and WS2.

We analyze the MSLP and 10-m wind anomalies from ERA5 over the region from 20°S to 80°N, 40°E to 170°E (Figure 5). There is a strong anticyclone originating from the Arctic region in the days leading up to the surge onset for WS1 (31 December 2020). The Siberian high reaches its peak strength on day -3 (Figure 5a) at which time the anomalies are between +35 and +40 hPa relative to climatology over a large area between 55°N and 80°N. On day -1 (Figure 5b), there is a southward intrusion of positive MSLP anomalies and a slight weakening of the Siberian high. At the same time, a low-pressure system to the east of the southward intrusion deepens (reaching close to -25 hPa), creating a zonal pressure gradient. This low-pressure system depicts an extratropical cyclone in the North Pacific. North-easterly to north-westerly winds begin to strengthen over the northern South China Sea and Philippine Sea from the southward propagation of the anticyclone associated with the pressure gradient. The north-easterly surge then affects the entire South China Sea on day +1 (Figure 5c), and the positive MSLP anomalies from the southward intrusion weaken while the low-pressure system deepens (reaching well

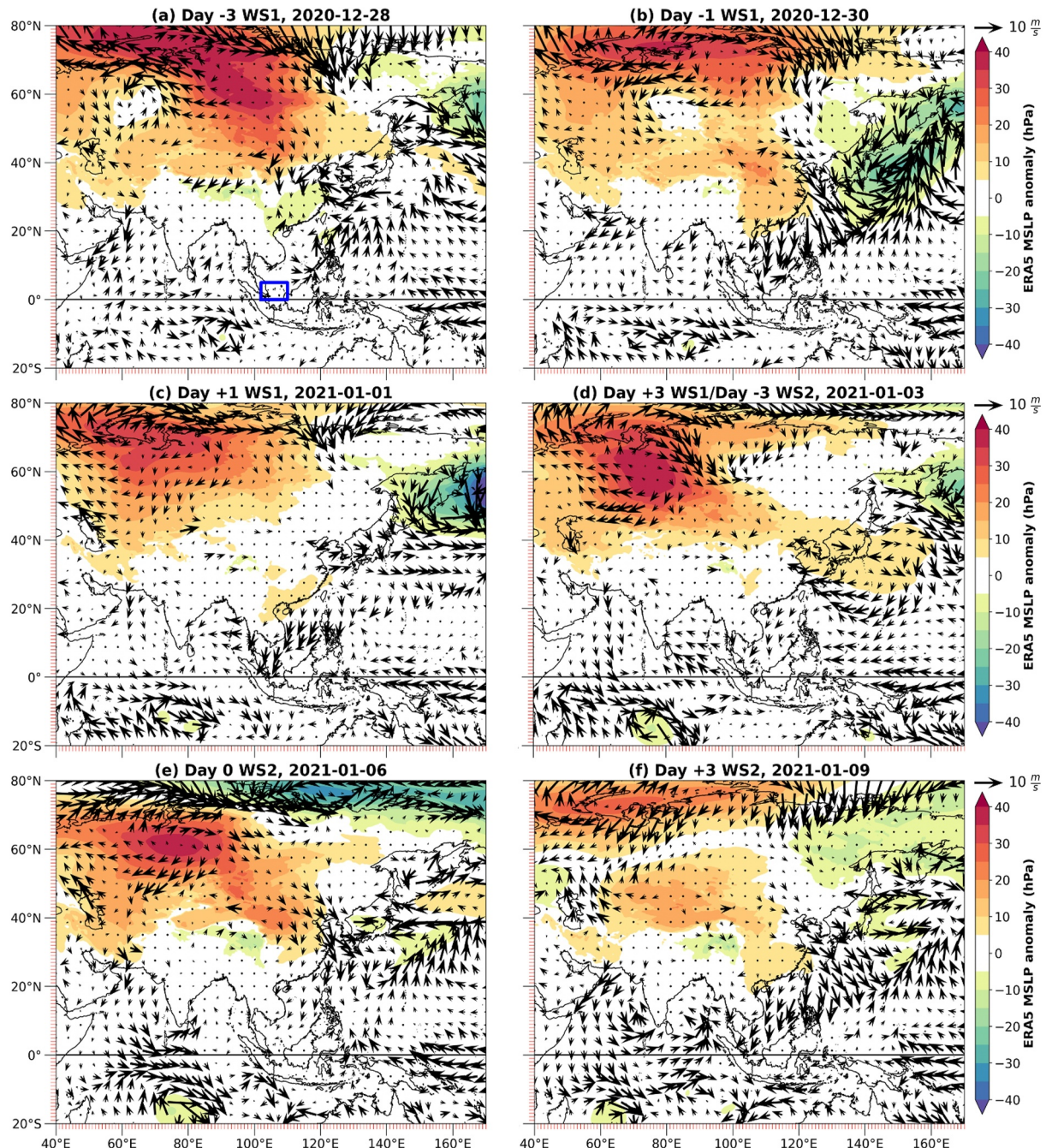


**Figure 5.** Daily mean ERA5 MSLP anomalies relative to the DJF 2000–2001 to 2019–2020 climatology for WS1 and WS2. (a) Day -3 on 28 December 2020, (b) day -1 on 30 December 2020, (c) day +1 on 1 January 2021, and (d) day +3 on 3 January 2021 with respect to the onset of WS1. (e) Day 0 on 6 January and (f) Day +3 on 9 January 2021 with respect to the onset of WS2. Daily mean 10-m horizontal wind anomaly vectors. The RRE domain is depicted by the blue box in panel (a).

below  $-40 \text{ hPa}$ ) and moves eastward. The anticyclone strengthens again on day +3 (Figure 5d) as WS1 weakens, which is also 3 days prior to the onset of WS2.

There is also a gradual southward intrusion and weakening of the Siberian high between day -3 and day 0 relative to WS2 (Figures 5d and 5e). Another extratropical cyclone develops to the east of the intrusion on day +1 (reaching close to  $-20 \text{ hPa}$ ; not shown), creating another zonal pressure gradient. On day +3 (Figure 5f), another weaker anticyclone with MSLP anomalies peaking close to  $+30 \text{ hPa}$  develops over the northern and western parts of the region. The southward intrusion that is associated with WS2 appears detached from the newly established

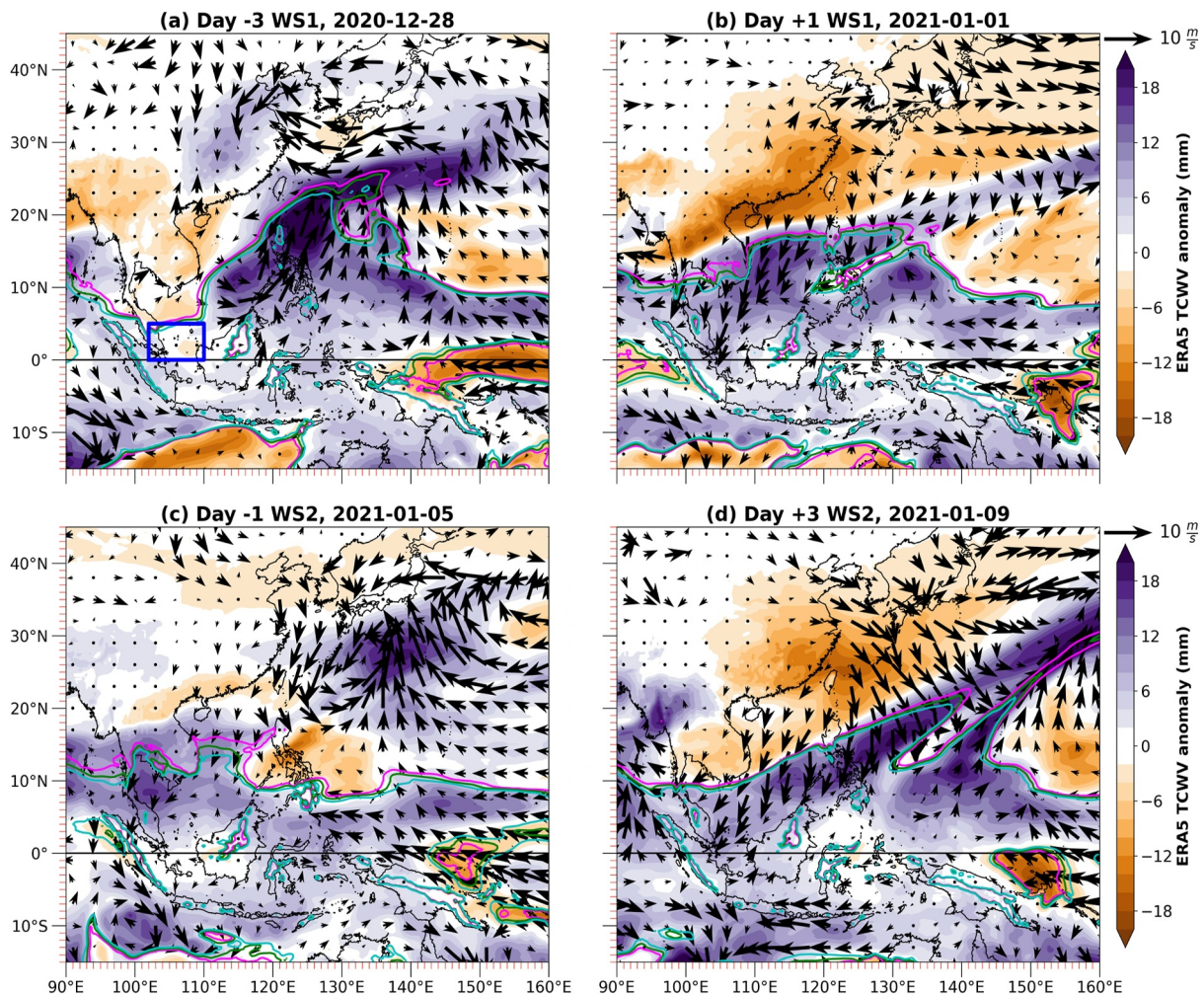


**Figure 6.** Daily mean ERA5 TCWV anomalies relative to the DJF 2000–2001 to 2019–2020 climatology for WS1 (top row) and WS2 (bottom row). (a) Day  $-3$  on 28 December 2020 and (b) day  $+1$  on 1 January 2021 with respect to the onset of WS1. (c) Day  $-1$  on 5 January and (d) Day  $+3$  on 9 January 2021 with respect to the onset of WS2. Daily mean 10-m horizontal wind anomaly vectors. Magenta, green, and cyan contours of TCWV are drawn at 46, 48, and 50 mm respectively. The RRE domain is depicted by the blue box in panel (a).

anticyclone, and continues to weaken and propagate southward (+5 to +20 hPa). The extratropical cyclone is also nearly dissipated, but the zonal pressure gradient still contributes to the north-easterly surge. WS2 is longer-lived compared to WS1, and finishes on day  $+6$  or 12 January (not shown). This could be attributed to the relatively slow weakening of the southward intrusion that prolongs the north-easterly surge flow.

TCWV anomalies from ERA5 are analyzed over a smaller region from  $15^{\circ}\text{S}$  to  $45^{\circ}\text{N}$ ,  $90^{\circ}\text{E}$ – $160^{\circ}\text{E}$  to focus more on the source and development of moist air over the South China Sea (Figure 6). There are strongly enhanced positive TCWV anomalies (peaking over +20 mm) where TCWV values are well over 50 mm between the Philippine Islands and Taiwan on day  $-3$  relative to the onset of WS1 (Figure 6a). The drier air from the north-easterly surge over the northernmost part of the South China Sea then creates a strong TCWV anomaly gradient (between  $-18$  and  $+18$  mm) with the moister air that advects southward over the equatorial South China Sea (day  $+1$  shown; Figure 6b). This gradient is associated with the contrast between the convection near the equator and drier surge air over the northern South China Sea (Tan et al., 2023). Moreover, the 48 mm TCWV contour that is based on the moist regime defined by Mapes et al. (2018) approximately separates the moister and drier airmasses.

Prior to the onset of WS2, there are positive TCWV anomalies over most of the South China Sea, including the RRE domain (day  $-1$  shown; Figure 6c). The strong TCWV gradient (reaching close to  $-16$  mm and over +20 mm) is re-established by day  $+3$  (Figure 6d), which is consistent with the surge being longer-lived and

developing more slowly. This also corresponds to the first extreme rainfall day in WS2. Moreover, the moisture gradient is still maintained even after the end of WS2 until the drier air over the northern South China Sea is advected toward the equatorial South China Sea by 17 January 2021 (not shown), which also marks the onset of the brief dry surge (see Figure 3a).

The positive TCWV anomalies are consistent with the MJO being primarily in Phase 3 over the equatorial region (see Figure 3b). The moist anomalies over the South China Sea leading up to WS2 are associated with the amplitude of the MJO being greater than 1 (i.e., an active MJO in the background), whereas the amplitude is less than 1 in WS1. Hence, the moist anomalies in WS1 are more attributable to the advection of moist air from near the Philippine Islands and Taiwan.

On the large scale, the wet surges of January 2021 are characterized by an anomalously strong Siberian high, as consistent with findings from Hai et al. (2017) and Ma et al. (2022). The southward intrusions of the anticyclone and extratropical cyclones to the east create a zonal pressure gradient, which strengthens the north-easterly to north-westerly winds over both the South China Sea and Philippine Sea (Kumar, 2021; Kumar et al., 2019; Xia et al., 2024). The north-easterly surge then affects the entire South China Sea. These circulation patterns are qualitatively consistent with the theory of geostrophic adjustment on an equatorial beta plane as first described by Lim and Chang (1981), where the winds turn from northerly to north-easterly as the Rossby wave group is established. Anomalous moist air is present between the Philippine Islands and Taiwan in the days prior to the onset of WS1, which advects southward along the South China Sea and is associated with the surge. Moreover, the moist background environment prior to WS2 coincides with the MJO being in Phase 3 with the amplitude being greater than 1.

## 5. Evaluation of the MetUM Forecasts

Before using the MetUM forecasts to examine the detailed structure and development of the cold surges in January 2021, we evaluate the degree to which the model successfully simulates the synoptic dynamics. This involves an evaluation of quantities including precipitation, TCWV and  $B_L$ ,  $\theta_e$ , and horizontal winds along the surge (i.e., along-transect winds).

### 5.1. Synoptic Spatial Structure

We begin by evaluating the MetUM forecasts on the synoptic scale for the entire month of January 2021 by plotting the daily mean composites of precipitation at 3-hourly intervals at the lead times from 12 to 33 hr in both the MetUM forecasts and GPM (Figures 7a and 7b). The horizontal winds at 925 hPa are evaluated against ERA5. The difference between the data sets is also plotted (Figure 7c). Overall, there is a wet bias in the MetUM forecasts (peaking well over  $+1.0 \text{ mm h}^{-1}$ ), particularly to the north-west coast of Borneo Island. Mass conservation has been implemented since December 2016 in the MetUM forecasts over Southeast Asia to reduce the wet bias (Zerroukat & Shipway, 2017). Another measure of the degree of agreement is the Relative Root Mean Square Error (RRMSE), which is a normalized measure of the differences between the MetUM forecasts and observations over all grid points. In other words, RRMSE is defined by the Root Mean Square Error (RMSE) divided by the normalized mean of the observed values. The overall precipitation structure in the MetUM forecasts appears to be in good agreement with GPM, where the RRMSE is approximately 0.61. The RRMSE for the zonal and meridional winds are approximately 0.18 and 0.16 respectively. This implies that the winds are in better agreement overall, and there is only a small region of weak easterly to north-easterly bias in the MetUM forecasts over Vietnam and Cambodia between  $10^\circ\text{N}$  and  $15^\circ\text{N}$ .

### 5.2. Temporal Structure Over the RRE Domain

We also evaluate the MetUM forecasts from 25 December 2020 to 10 February 2021 by comparing the timeseries of daily mean precipitation rate (Figure 8a), TCWV (Figure 8b), and  $B_L$  (Figure 8c) against GPM and ERA5. These quantities are averaged over the RRE domain. For TCWV, the average is only taken at the northernmost part of the RRE domain ( $5^\circ\text{N}$ ) but over the entire longitudinal range ( $102^\circ\text{E}$  to  $110^\circ\text{E}$ ) to identify the days where TCWV falls below 48 mm within the domain. This is because the dry surge air is advected from the north. In the MetUM forecasts, there are missing data on both 17 and 18 January 2021, and these gaps are reflected in the timeseries.

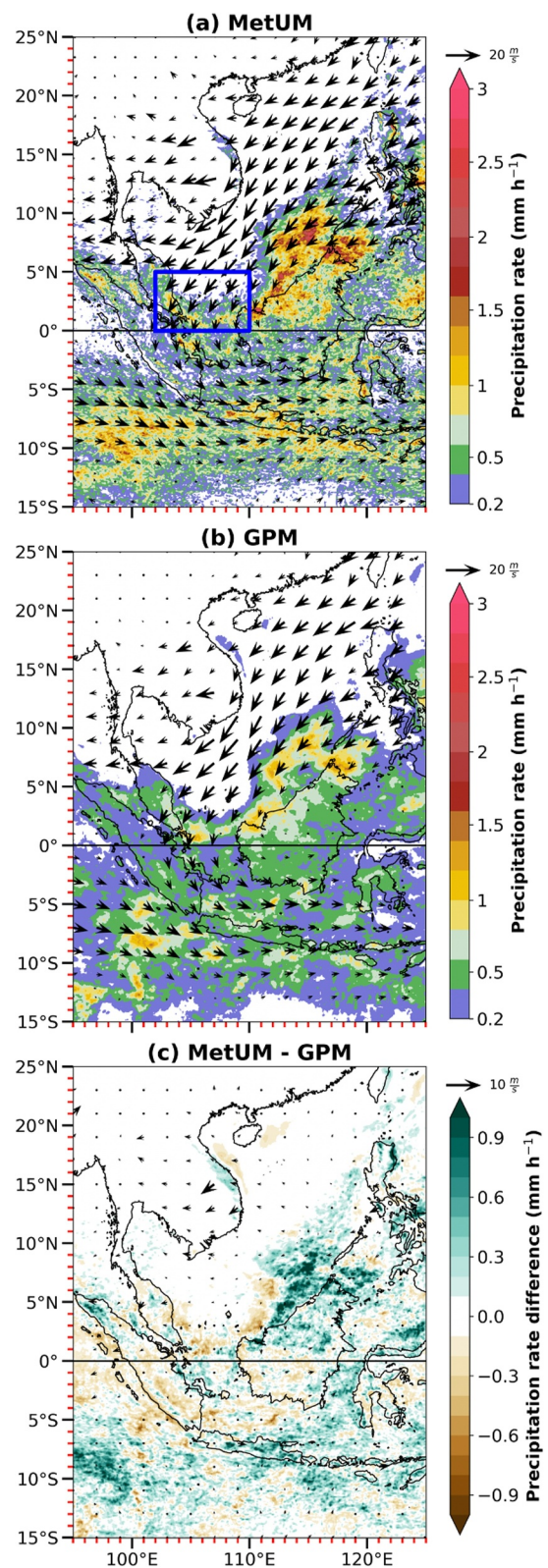


**Figure 7.** Model evaluation for the January 2021 mean composites of daily mean precipitation rate (shading) and 925 hPa horizontal winds (vectors). (a) MetUM precipitation, (b) GPM precipitation, and (c) MetUM—GPM. The MetUM data is regridded to the horizontal grid spacing of the GPM and ERA5 respectively in panel (c). The RRE domain is depicted by the blue box in panel (a).

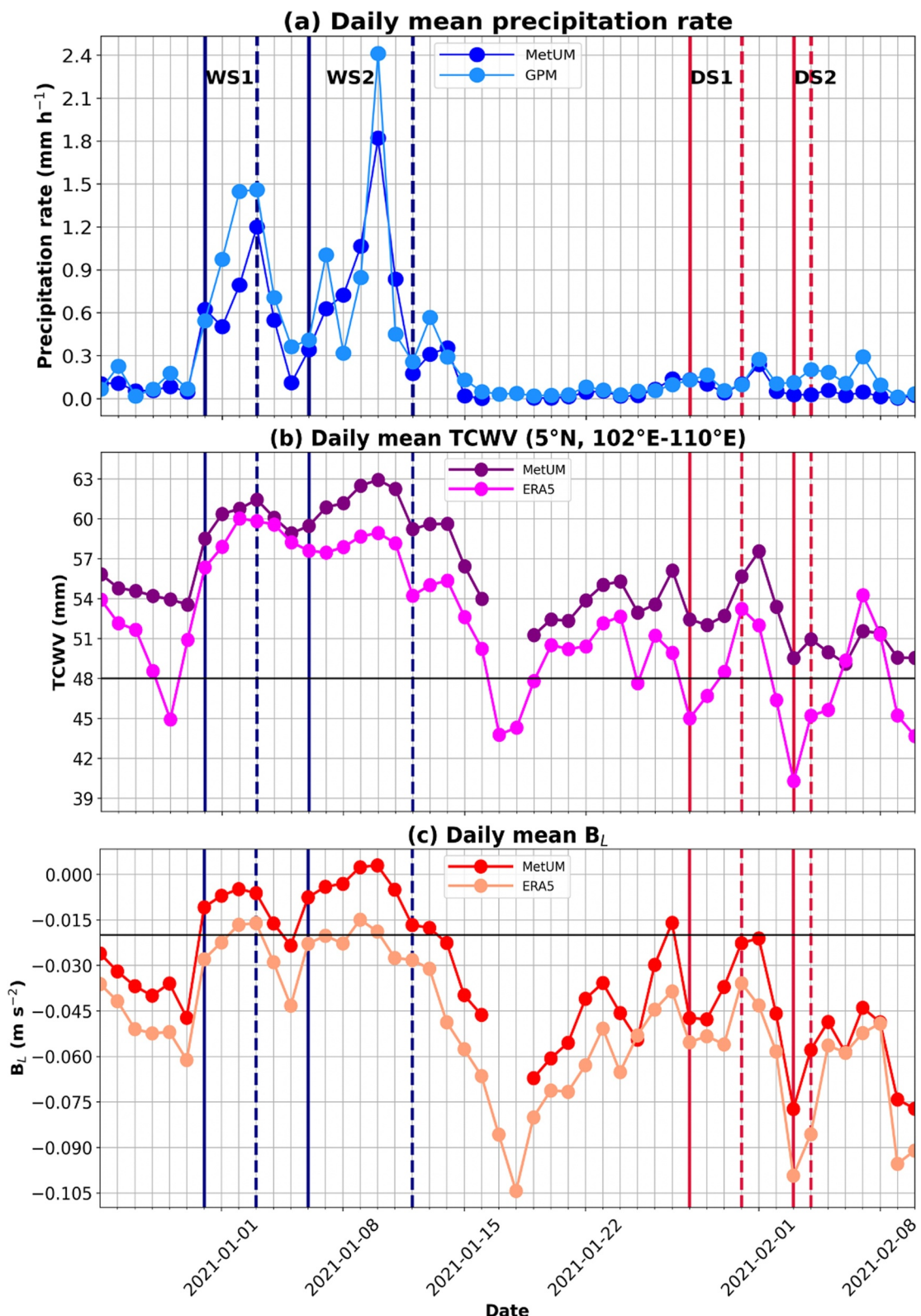


**Figure 8.** Timeseries of the daily mean (a) precipitation rate, (b) TCWV averaged longitudinally at  $5^\circ\text{N}$ , and (c)  $B_L$  from 25 December 2020–10 February 2021 over the RRE domain. Comparisons are made between the MetUM forecasts and GPM for precipitation rate, and between the model and ERA5 for the other two diagnostics. The solid black lines indicate the 48 mm and  $-0.02 \text{ m s}^{-2}$  thresholds for TCWV and  $B_L$ , respectively. The solid vertical lines indicate the days of surge onset for WS1 and WS2 (navy lines), and DS1 and DS2 (red lines). The dashed vertical lines indicate the end of each surge period.

In contrast to the synoptic evaluation, the MetUM forecasts underestimate the precipitation rate compared to GPM, particularly during the wet surges and the extreme rainfall days (except for 9 January 2021, and under-estimated rates reach close to  $-0.7 \text{ mm h}^{-1}$  on 2 January 2021). The underestimation here is likely attributable to the forecast error of convection initiation and organization. On the other hand, the MetUM forecasts overestimate TCWV and  $B_L$  compared to the reanalysis, implying a moist bias and higher instability in the forecasts, respectively. These results are consistent with the overestimation of precipitation over the larger region according to Figure 7c. The greatest overestimations of TCWV occur on the days where values fall below 48 mm in ERA5 but not in the MetUM forecasts, and is largest on 3 February 2021 at the onset of DS2 (close to +9 mm). The smallest overestimations occur from 31 December 2020 to 6 January 2021 (+0.5 to +2.5 mm). On most days,  $B_L$  values are consistently between +0.010 and +0.030  $\text{m s}^{-2}$  higher in the MetUM forecasts compared to ERA5.

The temporal structure is similar in both TCWV and  $B_L$ , and there is a clear contrast between the wet and dry surges. There is a sharp increase in both TCWV and  $B_L$  leading up to the surge onset between 29 and 31 December 2020. In the MetUM forecasts, TCWV increases from approximately 54 to 59 mm between 30 and 31 December (approximately 45 to 56 mm between 29 and 31 December in ERA5) and  $B_L$  increases from approximately  $-0.047$  to  $-0.011 \text{ m s}^{-2}$  (approximately  $-0.061$  to  $-0.028 \text{ m s}^{-2}$  in ERA5) between 30 and 31 December 2020. This implies a rapid moistening of the troposphere that provides favorable conditions for convection. The finding is also consistent with Figure 4 of Tan et al. (2023), where positive TCWV anomalies in wet surges generally strengthen following the onset of the surge. There are also peaks in both TCWV and  $B_L$  between 2 and 3 January, and between 9 and 10 January. TCWV peaks at approximately 61 and 63 mm on 3 and 10 January respectively (approximately 60 and 59 mm on 2 and 10 January respectively in ERA5), and  $B_L$  values are highest at approximately  $-0.005$  and  $0.003 \text{ m s}^{-2}$  on 2 and 10 January respectively ( $-0.016$  and  $-0.015 \text{ m s}^{-2}$  on 3 and 9 January respectively in ERA5). The transition to the dry surges occurs in the middle of January 2021 after the end of WS2. Here, TCWV values in ERA5 decrease from approximately 55 to 44 mm between 14 and 17 January, falling below the 48 mm moist regime value during the short dry surge between 17 and 18 January. TCWV also falls below 48 mm on most of the dry surge days, with the lowest value of approximately 40 mm on 3 February. Moreover,  $B_L$  values in ERA5 decrease from approximately  $-0.031$  to  $-0.104 \text{ m s}^{-2}$  between 13 and 18 January. We note that TCWV does not fall below 48 mm in the MetUM forecasts and this is associated with the moist bias.

### 5.3. Spatial and Temporal Structure Over the Transect Region

Looking at the spatial and temporal structure over the transect region (see orange box in Figure 1), the precipitation in WS1 and WS2 is generally in good agreement between the MetUM forecasts and GPM with a RRMSE of approximately 1.19 (Figures 9a and 9b). This is relatively high compared to the RRMSE value in Figure 7 since less averaging is required over the transect region compared to the January 2021 mean composites over a larger region. There is also a mixture of strong wet and dry biases in the MetUM forecasts (Figure 9c). The dry bias (reaching well below  $-10 \text{ mm h}^{-1}$ ) is largest on the extreme rainfall days of WS1 and WS2, which is consistent with the timeseries in Figure 8a. A relatively smaller region of wet bias (peaking well over  $+10 \text{ mm h}^{-1}$ ) follows the dry bias in both WS1 and WS2. These biases are located between the equator and approximately 2,800 km along the transect (approximately  $3^\circ\text{N}$ ), which is within the RRE domain. On the other hand, there is generally a wet bias along the South China Sea further to the north-east between 3,500 and 4,000 km along the transect (approximately  $8^\circ\text{N}$  and  $12^\circ\text{N}$  respectively), particularly during WS1. There are greater visible differences in the precipitation structure to the south of the equator in DS1 and DS2 due to its patchy nature. However, the biases are weaker in magnitude (peaking close to  $-8 \text{ mm h}^{-1}$  and  $+10 \text{ mm h}^{-1}$  for the dry and wet biases, respectively) since the convection is relatively weak.

We next evaluate the temporal structure of  $B_L$  (Figure 10). To our best knowledge, this quantity has not been evaluated before in the model forecasts. While the overall structure in both the MetUM forecasts (Figure 10a) and ERA5 (Figure 10b) is similar, the forecasts overestimate  $B_L$  (mostly between  $+0.02$  and  $+0.10 \text{ m s}^{-2}$ ) over most of the transect region (Figure 10c). However,  $B_L$  is underestimated ( $-0.02$  to  $-0.08 \text{ m s}^{-2}$ ) over the north-eastern part of the transect (northern South China Sea), particularly during WS1 and WS2. Therefore, there is a much larger region where  $B_L$  exceeds  $-0.02 \text{ m s}^{-2}$  near to the equator in the model forecasts. The RRMSE is approximately 0.22, which implies that despite the differences in magnitude, both data sets agree that the width of the convective region (taken to be where  $B_L$  exceeds  $-0.02 \text{ m s}^{-2}$ ) narrows to the south of the equator between the wet and dry surges. This result is consistent with the narrowing and southward movement of the ITCZ between the wet and dry phases of the boreal winter monsoon season over the Maritime Continent (McBride et al., 2015;

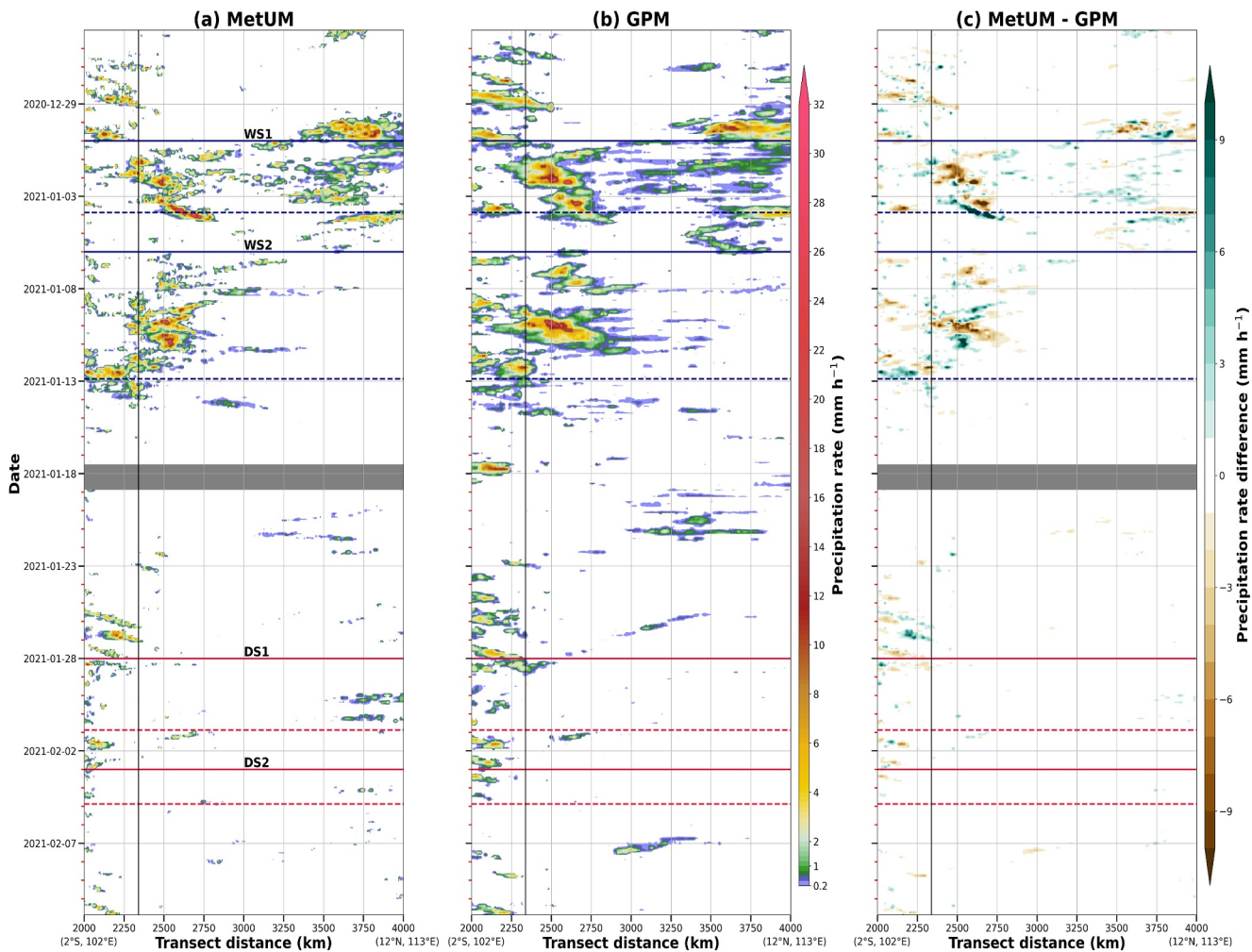


**Figure 9.** Model evaluation of the transect-averaged precipitation rate at 3-hourly resolution from 25 December 2020–10 February 2021. (a) MetUM, (b) GPM, and (c) MetUM—GPM. The MetUM data is re-gridded to the horizontal grid spacing of GPM in panel (c). Solid lines indicate the days of surge onset for WS1 and WS2 (navy lines), and DS1 and DS2 (red lines). Dashed lines mark the end of each surge period. The approximate location of the equator is marked by the vertical black line, and the transects are constructed from south-west to north-east moving left to right. A subset of the original transect is taken from 2,000 to 4,000 km, and the approximate latitude and longitude coordinates are specified on the  $x$ -axis at the start and end of the subset. Missing data in the MetUM forecasts between 17 and 18 January 2021 are shown in the gray shading.

Xavier et al., 2020). In the MetUM forecasts, the width of the convective region narrows from about 4,000 to 1,500 km between the wet and dry surges. The convective regions are patchier in ERA5 due to the consistently lower values of  $B_L$ . When comparing the two data sets, there are incoherent structures at approximately 2,000 km and 5,500 km along the transect (approximately 2°S and 23°N respectively) since the transects cross the islands of Sumatra and Taiwan respectively.

For the anomalies of TCWV (Figure 11), and anomalies of  $\theta_e$  and along-transect wind at 925 hPa (Figures 12 and 13 respectively), there is generally good structural agreement between the MetUM forecasts and ERA5. The RRMSE values here are approximately 0.30, 0.35, and 0.36 respectively. Overall, the contrasts between the wet and dry surges are consistent with the results in Tan et al. (2023).

In both the MetUM forecasts and ERA5, there is a strong moisture gradient in WS1 and WS2 based on the TCWV anomalies (Figures 11a and 11b respectively). In WS1, dry anomalies (reaching close to  $-18$  mm) extend from the north-eastern end of the transect (approximately 29°N) to about 5,000 km (approximately 19°N) along the transect before transitioning to moist anomalies (peaking close to  $+20$  mm) that reach to the equator. In WS2, the transition between negative and positive TCWV anomalies (reaching below  $-20$  mm and close to  $+14$  mm, respectively) is

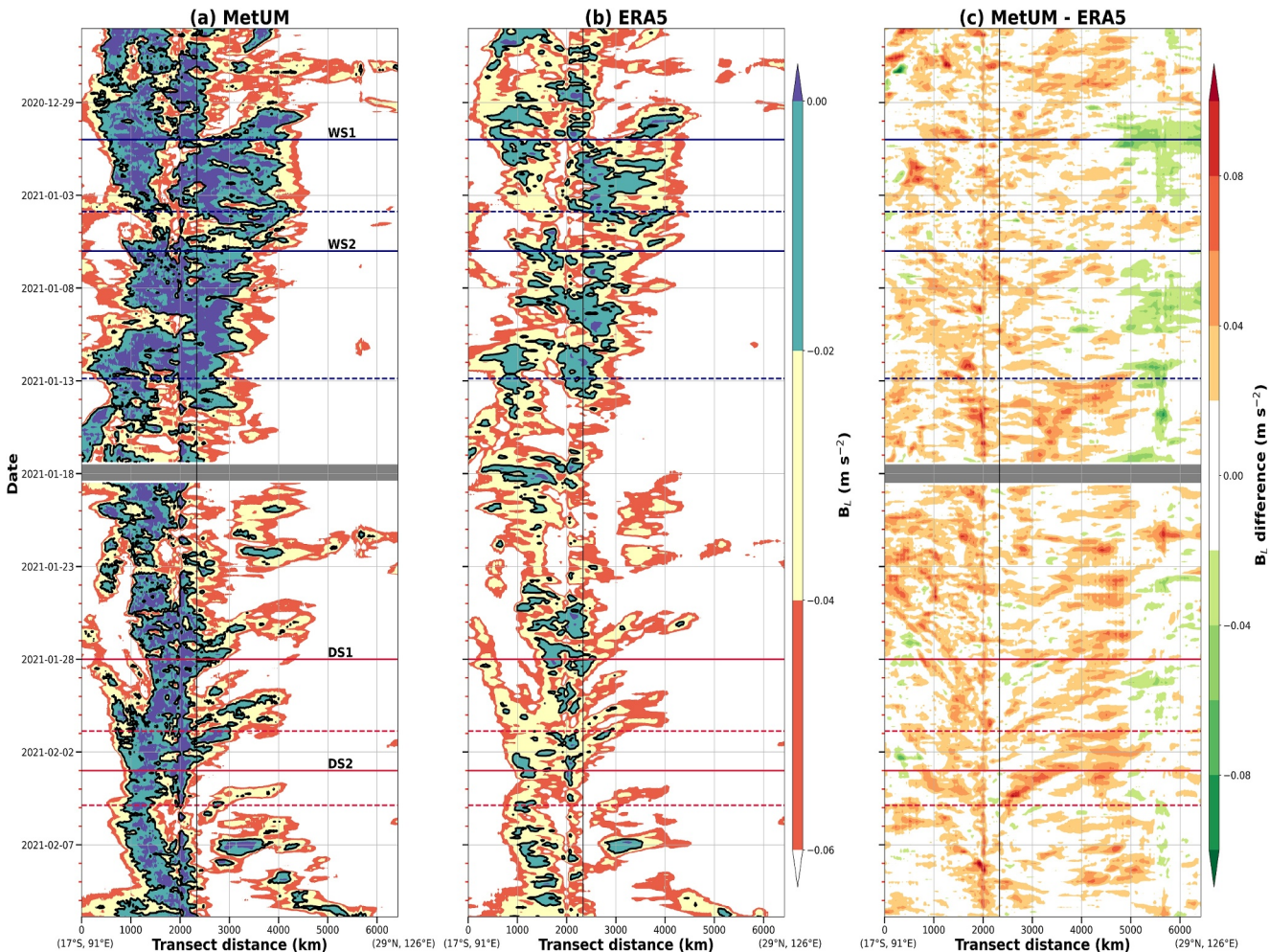


**Figure 10.** Model evaluation of the transect-averaged  $B_L$  at 3-hourly resolution from 25 December 2020–10 February 2021. (a) MetUM, (b) ERA5, and (c) MetUM–ERA5. The MetUM data is re-gridded to the horizontal grid spacing of ERA5 in panel (c). The black contours are drawn where  $B_L = -0.02 \text{ m s}^{-2}$ . Solid lines indicate the days of surge onset for WS1 and WS2 (navy), and DS1 and DS2 (red lines). Dashed lines mark the end of each surge period. The approximate location of the equator is marked by the vertical black line, and the transects are constructed from south-west to north-east moving left to right. The approximate latitude and longitude coordinates are specified on the x-axis at the start and end of the transect. Missing data in the MetUM forecasts between 17 and 18 January 2021 are shown in the gray shading.

found approximately 4,000 km (approximately 12°N) along the transect. The moist anomalies are stronger in WS1, although the dry anomalies in WS2 from the surge air are stronger. The dry anomalies in DS1 and DS2 reach the equator and are of similar strength to WS1. Moreover, the below-average moisture air is advected equatorward at approximately  $10 \text{ m s}^{-1}$ . The TCWV moisture gradient in the wet surges and the equatorward advection of drier air in the dry surges is consistent with Figure 4 of Tan et al. (2023). When comparing the two data sets, there is a mix of dry and wet anomaly differences (mostly between  $-6$  and  $+6 \text{ mm}$ ) between the MetUM forecasts and ERA5 (Figure 11c). The topographic incoherencies around Sumatra and Taiwan are less obvious compared to  $B_L$ . In WS1 and WS2, the dry biases in the MetUM forecasts ( $-2$  to  $-14 \text{ mm}$ ) close to 5,000 km along the transect are attributable to differing locations of the TCWV anomaly gradient.

For the anomalies of  $\theta_e$  at 925 hPa (Figures 12a and 12b), the cool and dry anomalies are much stronger over the northern South China Sea in the wet surges compared to the dry surges (reaching well below  $-20 \text{ K}$  toward the north-eastern end of the transect). Closer to the equator, there are warm and moist anomalies between  $+2$  and  $+6 \text{ K}$  in the wet surges. The transition from negative to positive anomalies occurs between 3,000 and 4,000 km along the transect (approximately 5°N and 12°N respectively) in WS1, and between 2,500 and 3,500 km (approximately 1°N and 8°N respectively) in WS2. Hence, the  $\theta_e$  anomaly gradients are closer to the equator

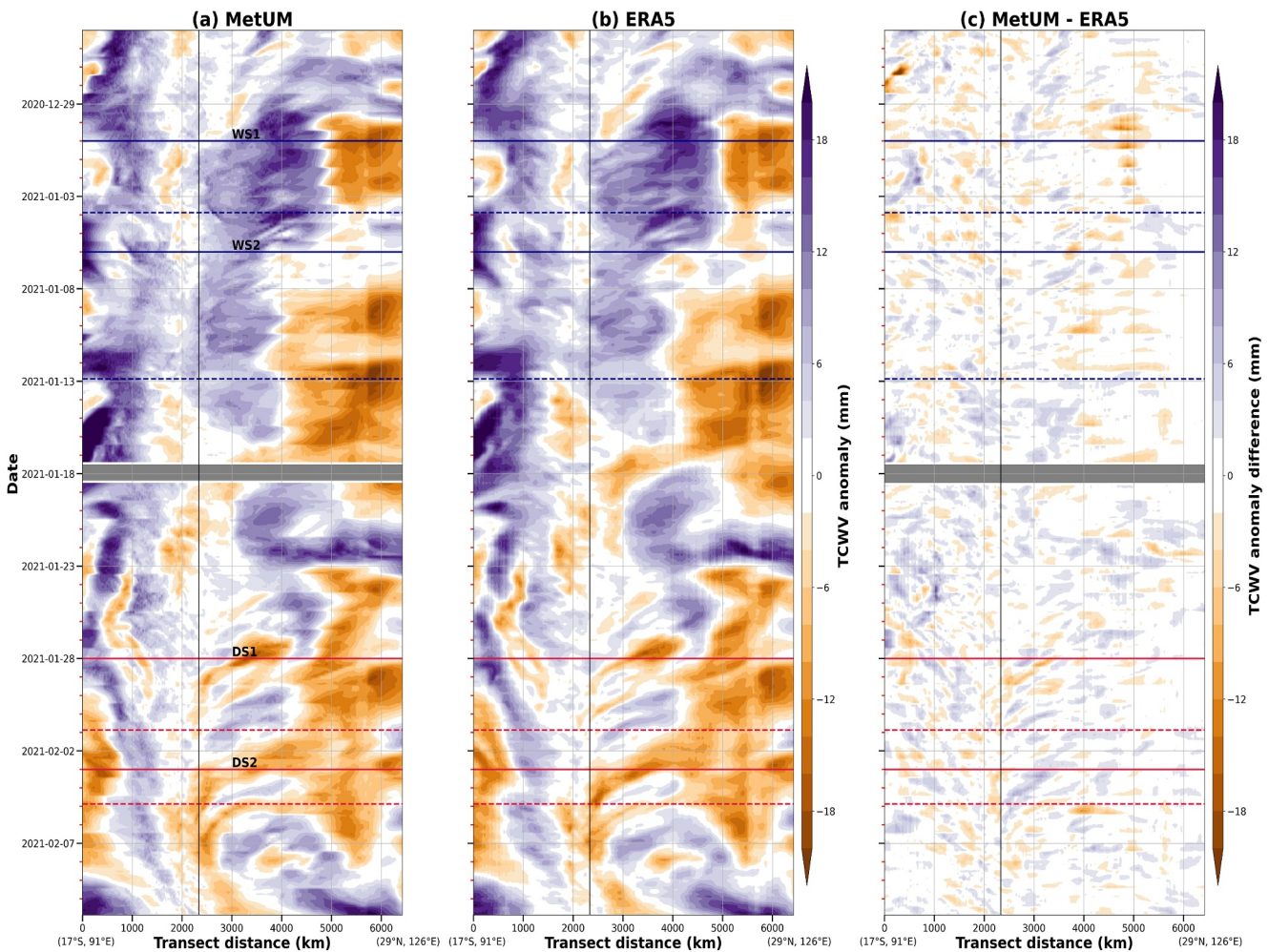


**Figure 11.** Model evaluation of the transect-averaged anomalies of TCWV at 3-hourly temporal resolution from 25 December 2020–10 February 2021. (a) MetUM, (b) ERA5, and (c) MetUM—ERA5. The MetUM data is re-gridded to the horizontal grid spacing of ERA5 in panel (c). Solid lines indicate the days of surge onset for WS1 and WS2 (navy lines), and DS1 and DS2 (red lines). Dashed lines mark the end of each surge period. The approximate location of the equator is marked by the vertical black line, and the transects are constructed from south-west to north-east moving left to right. The approximate latitude and longitude coordinates are specified on the  $x$ -axis at the start and end of the transect. Missing data in the MetUM forecasts between 17 and 18 January 2021 are shown in the gray shading.

compared to the TCWV anomaly gradients. In the dry surges, the cool and dry anomalies peak close to  $-20\text{ K}$  at the north-eastern end of the transect and are advected toward the equatorial South China Sea at similar speeds to the TCWV anomalies (approximately  $10\text{ m s}^{-1}$ ). The topography over Sumatra is also associated with positive  $\theta_e$  anomaly biases in the MetUM forecasts compared to ERA5 (between  $+2$  and  $+18\text{ K}$ ; Figure 12c).

Looking at the along-transect wind anomalies at 925 hPa (Figures 13a and 13b), the north-easterly surge anomalies in the wet surges (reaching close to  $-16\text{ m s}^{-1}$ ) are much stronger than in the dry surges (reaching close to  $-10\text{ m s}^{-1}$ ). These patterns are consistent with the negative anomalies of TCWV and  $\theta_e$  toward the north-eastern end of the transect, and a stronger Siberian high outflow prior to the wet surges compared to the dry surges. The winds propagate about twice the speed of the advection of both the TCWV and  $\theta_e$  anomalies (approximately  $20\text{ m s}^{-1}$ ). As described in Tan et al. (2023), these results are consistent with the theoretical framework of Lim and Chang (1981) and findings by Chang et al. (1983), where the equatorward propagation of the surge is associated with increased surface pressure from the Siberian high and gravity-wave type motions. These are followed by a decrease in surface temperature and subsequently, a strengthening of the surge winds. Hence, both the wet and dry cold surges are characterized by the faster propagation speed of north-easterly winds relative to the slower advection velocity of colder and drier air from the surge. Like the TCWV anomalies, there is a mix of positive and negative biases in the along-transect winds (mostly between  $-4$  and  $+4\text{ m s}^{-1}$ ; Figure 13c).

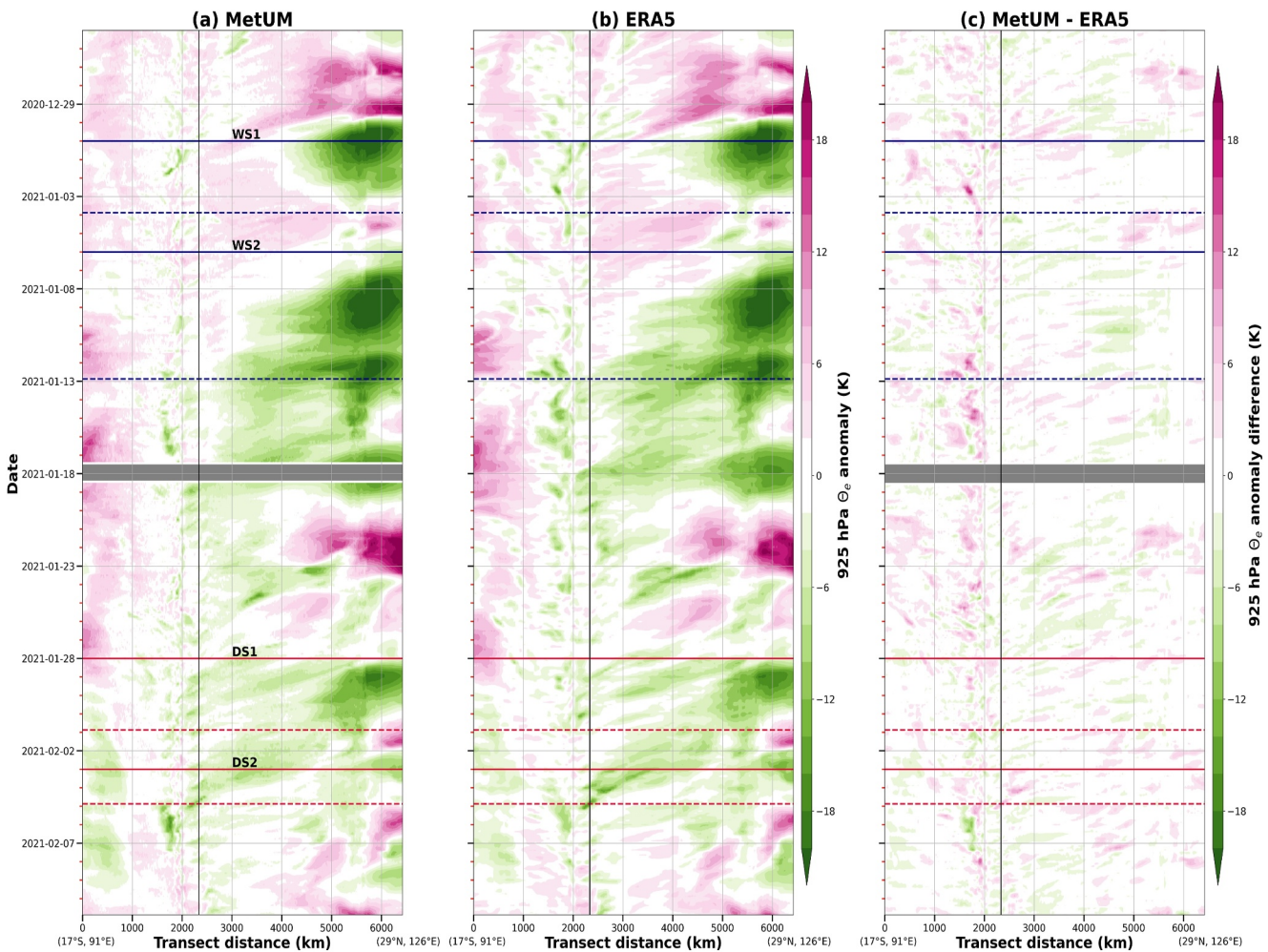


**Figure 12.** Model evaluation of the transect-averaged anomalies of 925 hPa  $\theta_e$  at 3-hourly temporal resolution from 25 December 2020–10 February 2021. (a) MetUM, (b) ERA5, and (c) MetUM—ERA5. The MetUM data is re-gridded to the horizontal grid spacing of ERA5 in panel (c). Solid lines indicate the days of surge onset for WS1 and WS2 (navy lines), and DS1 and DS2 (red lines). Dashed lines mark the end of each surge period. The approximate location of the equator is marked by the vertical black line, and the transects are constructed from south-west to north-east moving left to right. The approximate latitude and longitude coordinates are specified on the  $x$ -axis at the start and end of the transect. Missing data in the MetUM forecasts between 17 and 18 January 2021 are shown in the gray shading.

Over the transect region, the model forecasts are in good agreement with the reanalysis and observations. The RRMSE is highest for precipitation due to the mixture of strong wet and dry biases in the model forecasts. In contrast, the RRMSE is lowest for  $B_L$  as both the model and reanalysis data sets agree that the width of the convective region narrows to the south of the equator between the wet and dry surges. Moreover, the fields appear to be continuous between the lead times of 33 and 12 hr when stitching the forecasts together, which suggests that the model forecasts perform well at these selected lead times on the synoptic scale.

## 6. Mesoscale Analysis of WS1 in the MetUM Forecasts

In this section, we focus on the RRE domain when utilizing the high-resolution of the MetUM forecasts to analyze the mesoscale aspects of WS1 that cannot otherwise be deduced from reanalysis and observations as their horizontal grid spacing is too coarse. Here, only WS1 is analyzed due to the many similarities with WS2.

### 6.1. Horizontal and Vertical Structure of the Surge Leading Edge

We begin by analyzing the structure of the leading edge in WS1 at the time of the surge onset (Figure 14). Maps of  $B_L$  over the RRE domain and anomalies of  $\theta_e$  and potential temperature ( $\theta$ ) in the vertical are shown on 30 December 2020 at 2300 LST and 31 December 2020 at 0500 LST. At the earlier time, values of  $B_L$  are below

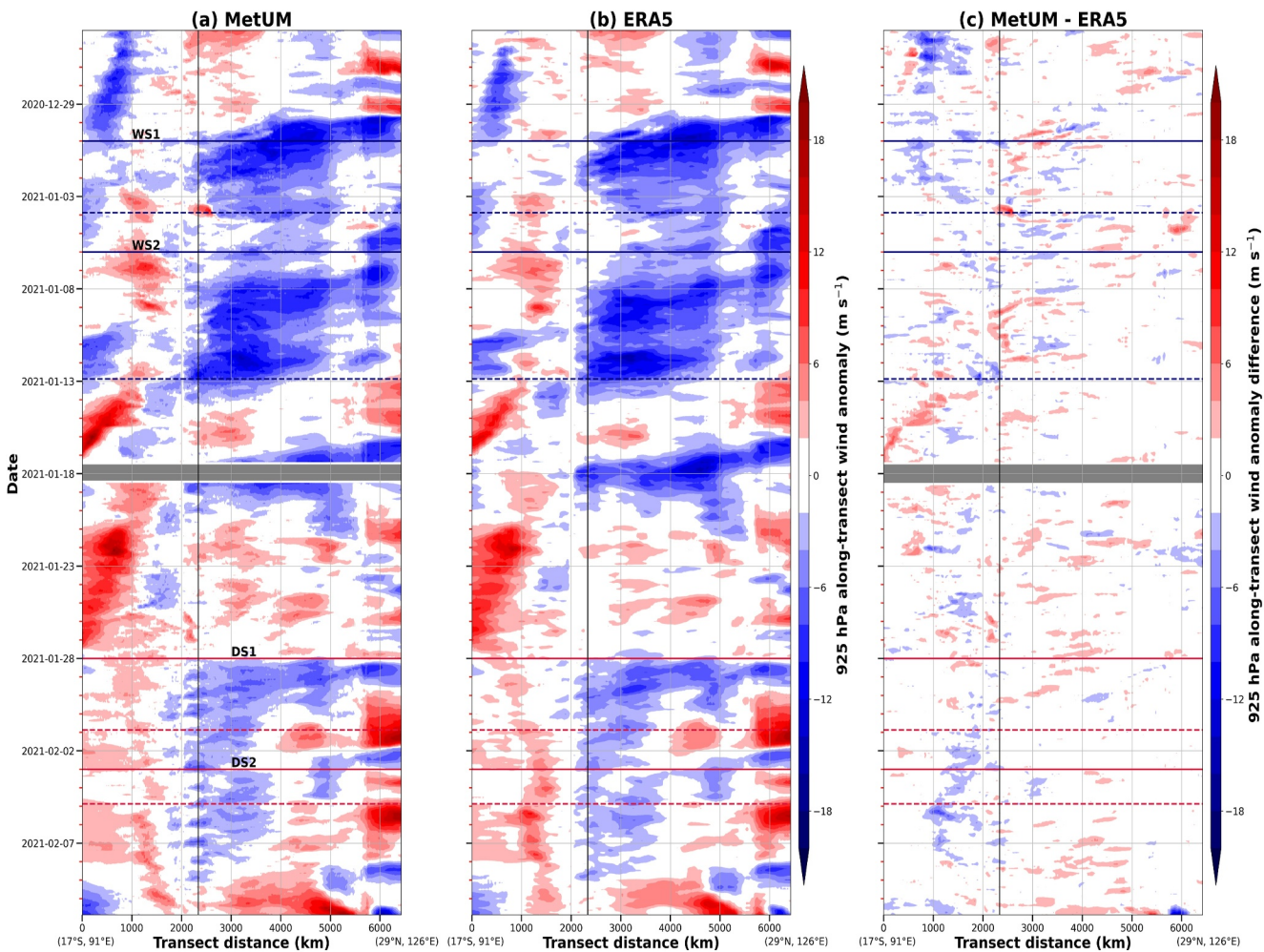


**Figure 13.** Model evaluation of the transect-averaged anomalies of 925 hPa along-transect winds at 3-hourly temporal resolution from 25 December 2020–10 February 2021. (a) MetUM, (b) ERA5, and (c) MetUM—ERA5. The MetUM data is re-gridded to the horizontal grid spacing of ERA5 in panel (c). Along-transect winds are negative moving north-east to south-west. Solid lines indicate the days of surge onset for WS1 and WS2 (navy lines), and DS1 and DS2 (red lines). Dashed lines mark the end of each surge period. The approximate location of the equator is marked by the vertical black line, and the transects are constructed from south-west to north-east moving left to right. The approximate latitude and longitude coordinates are specified on the x-axis at the start and end of the transect. Missing data in the MetUM forecasts between 17 and 18 January 2021 are shown in the gray shading.

$-0.02 \text{ m s}^{-2}$  over most of the domain with the lowest values reaching below  $-0.10 \text{ m s}^{-2}$  (Figure 14a). This region of relatively low  $B_L$  marks the leading edge of the incoming surge at approximately  $3^\circ\text{N}$  on average based on the abrupt weakening of northerly wind anomalies. At the latter time, the large area of relatively low  $B_L$  is replaced by values exceeding  $-0.02 \text{ m s}^{-2}$  over much of the domain, including parts of the leading edge that has moved equatorward to approximately  $2^\circ\text{N}$  (Figure 14b). The advection of these higher values of  $B_L$  coincides with the strengthening of the surge winds. In other words, the onset of the surge is associated with the advection of moister free-tropospheric air that enables deep convection to develop at the leading edge of the surge. This result is consistent with the TCWV analysis on the synoptic scale in Figures 6 and 11. As the surge subsequently strengthens over the RRE domain, the areas in which  $B_L$  exceeds  $-0.02 \text{ m s}^{-2}$  becomes widespread and is associated with the organization and deepening of the convection (not shown).

Vertical sections of the anomalies of  $\theta_e$  (Figures 14c and 14d) and  $\theta$  (Figures 14e and 14f) are plotted at 3-hourly intervals from 1,000 to 300 hPa over the RRE domain. Due to the northerly wind anomalies and quasi meridional propagation of the leading edge in the plan view maps, we take the average of 7 north-south cross sections from  $105^\circ\text{E}$  to  $108^\circ\text{E}$  at  $0.5^\circ$  intervals for some consistency with the south-west to north-east transects. We also use the hydrostatic approximation to convert W to  $\omega$ , which we exaggerate by a factor of 10 for clarity in plotting.

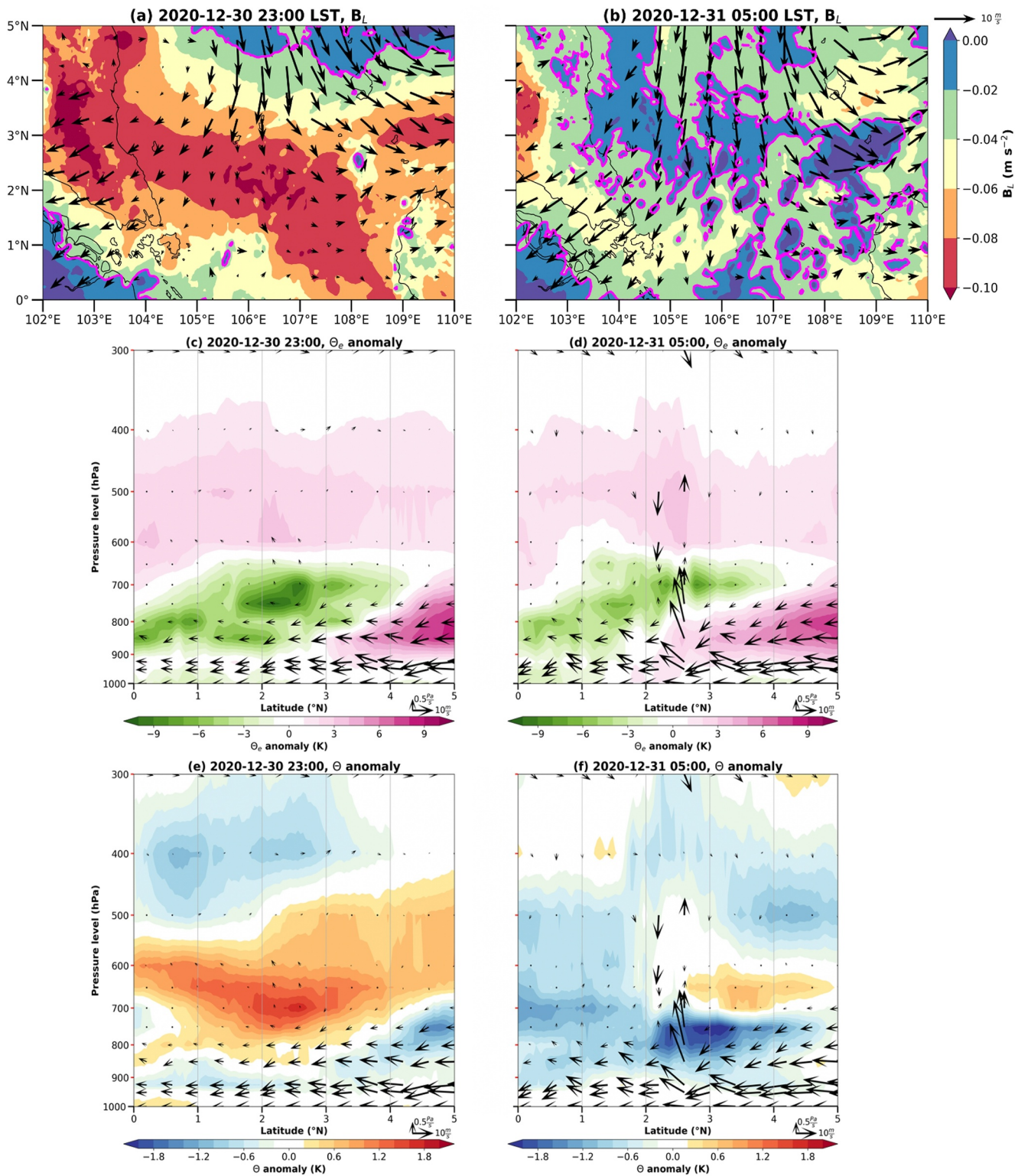


**Figure 14.** (a, b) Horizontal structure of  $B_L$  from the MetUM forecasts over the RRE domain for WS1. Daily mean 925 hPa horizontal wind anomaly vectors. The magenta contours are drawn where  $B_L$  is  $-0.02 \text{ m s}^{-2}$ . Cross-section averaged anomalies of (c, d)  $\theta_e$  and (e, f)  $\theta$  in the vertical from the MetUM forecasts over the RRE domain latitudes for WS1. Vectors depict the magnitudes of daily mean meridional winds and  $\omega$ .  $\omega$  is exaggerated by a factor of 10. Left column: 30 December 2020 at 2300 LST and right column: 31 December 2020 at 0500 LST.

Between 2300 LST on 30 December and 0500 LST on 31 December, positive anomalies of  $\theta_e$  in the lower to mid troposphere (peaking close to +8 K between 950 and 650 hPa) are advected equatorward (Figures 14c and 14d). These positive anomalies begin to replace the negative anomalies that previously covered most of the RRE domain within the lower-to-mid troposphere. The regions of transition between the positive and negative anomalies of  $\theta_e$  also correspond to the latitude of the leading edge of the surge in the horizontal structure of  $B_L$  (approximately 3°N in the earlier time and 2°N in the latter time). In the latter time, there is also upward motion just to the north of the leading edge between 2°N and 3°N that marks the initiation of convection. Subsequently, the positive anomalies spread over the entire domain and deepen as convective activity increases (see Figure 15). Moreover, there is the appearance of a weak gravity-current-like structure as the moister air is advected equatorward. The resemblance of this structure is further evident in the negative anomalies of  $\theta$  at the lower levels and positive anomalies above. In the earlier time (Figure 14e), the cold anomalies lie between 950 and 700 hPa (-0.2 to -1.6 K) whereas the warm anomalies are between 850 and 450 hPa (peaking close to +1.8 K around 700 hPa). The opposing signs of  $\theta_e$  and  $\theta$  imply that cooler and moister air from the surge begins to replace the warmer and drier air in the domain. The widespread warm mid-tropospheric anomalies weaken and retreat northward (+0.2 to +0.8 K between 700 and 600 hPa) and are replaced by cold anomalies that reach below -2 K at 750 hPa at the latter time (Figure 14f). However, the spatial scale of the gravity-current-like head is about 200–300 km, which is too large for a gravity current that is normally on the order of 10 km or less (Smith & Reeder, 1988).

## 6.2. Horizontal and Vertical Structure of the Convection

To better understand the mesoscale structure and dynamics of the convection in WS1 in the MetUM forecasts, we analyze the precipitation and horizontal winds at 925 hPa over the RRE domain at 3-hourly intervals (Figures 15a, 15b and 15c). Selected 3-hr times (21-hr apart) between 31 December 2020 and 2 January 2021 are plotted to highlight the important mesoscale features in the spatial structure and development of the surge. These specific times are 2300 LST on 31 December 2020, 2000 LST on 1 January 2021, and 1700 LST on 2 January 2021. They are chosen as they best convey the mesoscale development of the surge. We also analyze the southwest-to-northeast transect-averaged anomalies of  $\theta_e$  in the vertical at the corresponding times (Figures 15d, 15e and 15f). A subset region of the transect is taken between 2,200 and 3,000 km (approximately 1.0°S and 4.7°N respectively) to analyze the vertical structure of the surge and its associated convection. It is important to note that the discontinuities in lead time from 33 to 12 hr between 1700 LST and 2000 LST when stitching the forecasts together are more noticeable on the mesoscale, and are a limitation in the use of the daily initialized forecasts. Table 3 provides a chronology of the mesoscale events of importance to WS1.

At 2300 LST on 31 December 2020, the north-easterly surge winds cover most of the RRE domain, and the convection at the leading edge is organized and oriented northwest-to-southeast (Figure 15a). A non-stationary cyclonic anomaly develops to the east of the north-easterly surge winds, which is most likely a local cyclonic circulation. This cyclonic circulation is associated with more intense convection that follows its curvature. The surge and its leading edge, the convection, and the cyclonic anomaly propagate toward the south and west of the domain. By 2000 LST on 1 January 2021 (Figure 15b), the first band of convection weakens, and another line of convection develops as the surge winds strengthen further. The convection at the leading edge of the surge reaches its peak at 17:00 LST on 2 January 2021 (Figure 15c), and is associated with the south-west movement of the cyclonic circulation toward Singapore. Precipitation rates locally peak close to 85 mm h<sup>-1</sup> and the organized line of convection lies to the south-western flank of the cyclonic circulation over Singapore and the surrounding region. Therefore, the strengthening of the north-easterly winds and organization of convection within the RRE domain is attributable to the combination of the cold surge and local tropical low. Moreover, the tropical low that develops to the east of the strong surge winds tilts toward the north and west and weakens with increasing height, reaching up to approximately 500 hPa (not shown).

In the vertical, the warm and moist anomalies of  $\theta_e$  (+1 to +8 K) are already widespread in the first time, covering most of the troposphere and the plotting region (Figure 15d). These anomalies are associated with ascent from the convection. Precipitation rates peak at approximately 5.5 and 6.9 mm h<sup>-1</sup> close to 2,500 and 2,800 km (close to 1.1°N and 3.3°N respectively) along the transect, respectively. There is also a weak vertical deformation of the  $\theta_e$  isentropes where warmer and moister air corresponds to the areas of convection while cooler and drier air is found on either side. In the middle time (Figure 15e), the development of the second round of convection is marked by the equatorward advection and deepening of stronger moist anomalies (+5 to +9 K between 900 and 600 hPa). The deformation of  $\theta_e$  isentropes occurs just to the north of the equator and corresponds to the precipitation peak

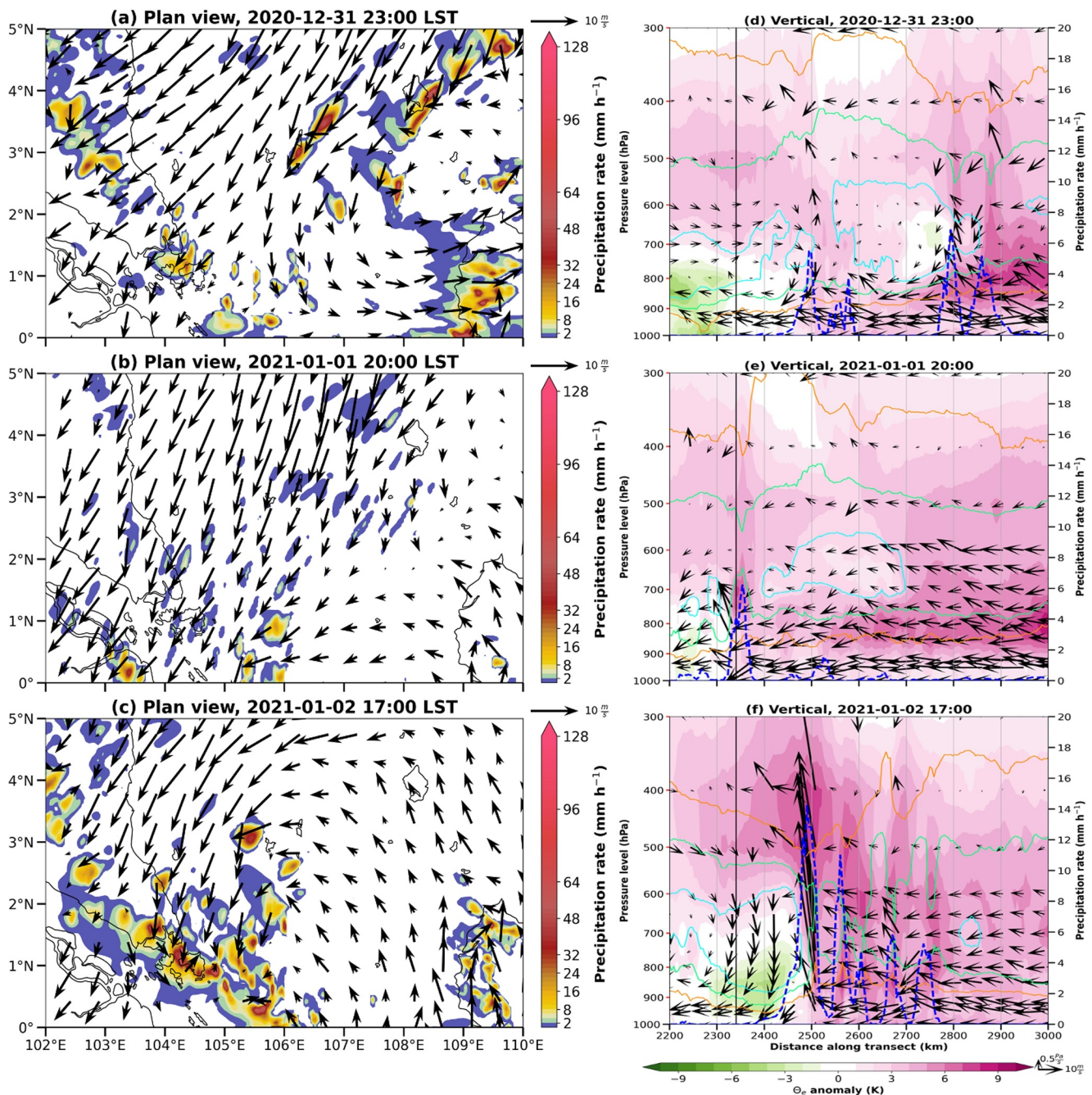


**Figure 15.** Left column: Horizontal structure of precipitation from the MetUM forecasts over the RRE domain for WS1. Daily mean 925 hPa horizontal wind anomaly vectors. Right column: Transect-averaged anomalies of  $\theta_e$  in the vertical from the MetUM forecasts for WS1. The dashed blue line shows the along-transect precipitation. Cyan, green, and orange isentropes of  $\theta_e$  are drawn at 340, 343, and 346 K respectively. Vectors depict the magnitudes of daily mean along-transect winds and  $\omega$ .  $\omega$  is exaggerated by a factor of 10. The approximate location of the equator is marked by the vertical black line, and the transects are constructed from south-west to north-east moving left to right. A subset region is taken from 2200 to 3,000 km along the transect. (a, d) 31 December 2020 at 2300 LST, (b, e) 1 January 2021 at 2000 LST, and (c, f) 2 January 2021 at 1700 LST.

of approximately  $4.9 \text{ mm h}^{-1}$ . The stronger deformation here implies that the convection transports moister air from the boundary layer upward (where the 343 K contour rises from between 850 and 800 hPa to approximately 650 hPa). At the final time when the surge reaches its peak (Figure 15f), the location of the heaviest precipitation (peaking at approximately  $14.2 \text{ mm h}^{-1}$ ) coincides with the location of maximum ascent, and strongest positive  $\theta_e$  anomalies (peaking close to  $+8 \text{ K}$ ) and deformation of  $\theta_e$  isentropes between 2,500 and 2,600 km (approximately

**Table 3**  
*Summary of Mesoscale Events Concerning WS1*

Dates (Day relative to surge onset)	Mesoscale events of importance to WS1
31 December 2020 (Day 0 WS1)	Surge onset for WS1. North-easterly surge winds strengthen and positive $\theta_e$ anomalies become widespread and deepen. Initiation and organization of convection at the leading edge associated with a local cyclonic circulation to the east.
1 January 2021 (Day +1)	Convection at the leading edge propagates toward the south-west of the domain and weakens. Another round of strengthening surge winds and development of convection occurs toward the end of the day. First observed extreme rainfall day.
2 January 2021 (Day +2)	The cold surge and its leading edge and the convection are fully established. Strong positive $\theta_e$ anomalies and a local cyclonic circulation. Second observed extreme rainfall day.
3 January 2021 (Day +3)	Final day of WS1. Convection and local cyclonic circulation move westward (not shown in figure). Positive $\theta_e$ anomalies are maintained.
4 January 2021 (non-surge day)	Another anomalous band of organized convection associated with the convergence of southerlies and easterlies in the MetUM forecasts, and strong positive $\theta_e$ anomalies. Convection dissipates rapidly from the afternoon hours.

1.1°N and 1.9°N respectively) along the transect. A region of descent associated with negative  $\theta_e$  anomalies ( $-1$  to  $-4$  K) to the south-west of the convective peak are likely associated with downdrafts from the convection and topography from Sumatra Island close to and at the equator. The values of  $\theta_e$  range from below 340 K associated with the downdrafts to close to 346 K at the center of the convection, producing a  $\theta_e$  gradient of over 6 K.

Between the nocturnal and morning hours of 3 and 4 January 2021 (0500 LST on 4 January shown; Figure 16a), there is a strong convergence of southerly anomalies between the equator and approximately 2.5°N and easterly anomalies over the northern half of the domain. This is associated with another line of organized convection that is not part of WS1 which finishes on 3 January. The anomalous band of convection is not found in the GPM observations (see the wet bias in Figure 9c). The convection is also reflected in the strongly positive anomalies of  $\theta_e$  in the vertical (peaking over  $+10$  K) that corresponds to precipitation rates along the transect peaking well over  $20 \text{ mm h}^{-1}$  (Figure 16b). Values of  $\theta_e$  exceed 346 K at the center of the convection and reaches below 340 K to the south-west. According to Ferrett et al. (2021), the skill of the MetUM forecasts tends to be lowest at night when the precipitation is offshore.

Overall, WS1 is characterized by an anomalously strong Siberian high that creates a zonal pressure gradient with low-pressure anomalies to the east, resulting in the strengthening of cold surge winds over the South China Sea and subsequently, the initiation and organization of deep convection over the equatorial region. Rainfall rates in the model forecasts are locally extreme over Singapore and its surroundings on 2 January 2021, which is consistent with the second extreme rainfall day according to the SRE definition. The anomalous band of convection between the nocturnal and morning hours of 3 and 4 January in the model forecasts is neither associated with the surge nor found in the GPM observations.

## 7. Conclusions

In this paper, we used a combination of observations, reanalysis, and high-resolution model forecasts from the MetUM to investigate the synoptic and mesoscale structures and development of the January 2021 cold surges. We particularly focused on the wet surge between 31 December 2020 and 3 January 2021, which is denoted as WS1, when utilizing the high-resolution of the model forecasts to understand the mesoscale processes. The MetUM forecasts were evaluated against the observations and reanalysis. Moreover, the wet surges were studied in the context of extreme rainfall over Singapore, which is an extension of the dry and wet surge categories defined in Tan et al. (2023).

Both WS1 and WS2 fall within the wet surge category over the precipitation (or RRE) domain when compared to the long-term composites. Based on the SRE definition, there are four extreme rainfall days (two in each surge). Therefore, the rainfall is locally extreme over Singapore and the surrounding region, but not the RRE domain (where only 1 out of 11 wet surge days is considered extreme). In other words, intense convective activity associated with these wet surges is highly localized. When analyzing the precipitation-buoyancy relationship, we

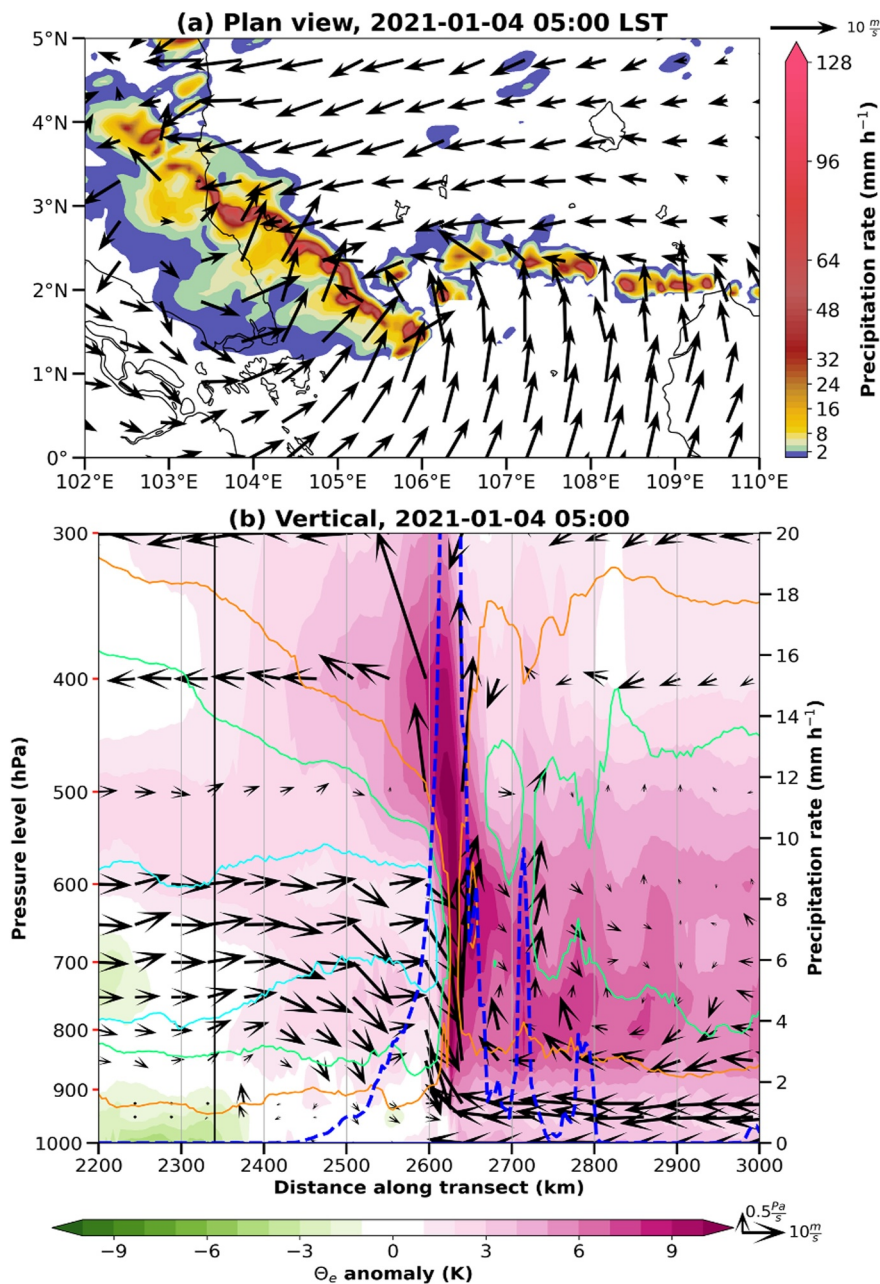


**Figure 16.** (a) Horizontal structure of precipitation from the MetUM forecasts over the precipitation domain at 0500 LST on 4 January 2021. Daily mean 925 hPa horizontal wind anomaly vectors. (b) Transect-averaged anomalies of  $\theta_e$  in the vertical from the MetUM forecasts at the same time. The dashed blue line shows the along-transect precipitation. Cyan, green, and orange isentropes of  $\theta_e$  are drawn at 340, 343, and 346 K respectively. Vectors depict the magnitudes of daily mean along-transect winds and  $\omega$ .  $\omega$  is exaggerated by a factor of 10. The approximate location of the equator is marked by the vertical black line, and the transects are constructed from south-west to north-east moving left to right. A subset region is taken from 2,200 to 3,000 km along the transect.

find that these extreme rainfall days are characterized by a moister free troposphere that allows convection to penetrate through the lower troposphere. Moreover, our results suggest that the precipitation-buoyancy relationship does not hold as strongly over a local area compared to the larger scale.

On the large-scale, both the wet surges are characterized by anomalously positive MSLP anomalies over Siberia prior to surge onset (peaking on day -3), and the resultant surge winds are stronger than in the dry surges. Southward intrusions of the Siberian high and extratropical cyclones to the east create a zonal pressure gradient

that is associated with the strengthening surge winds over both the Philippine Sea and northern South China Sea. Prior to the onset of WS1, anomalously moist air between the Philippine Islands and Taiwan advects southward along the South China Sea. The moist background environment prior to the onset of WS2 coincides with the MJO being in Phase 3 and the amplitude being greater than 1.

On the mesoscale for WS1, the organization of convection at the leading edge of the surge within the RRE domain are attributable to the combination of the cold surge and local tropical low. The strengthening surge winds also coincide with the advection of moist air, and the spreading and deepening of positive  $\theta_e$  anomalies. The heaviest precipitation coincides with the locations of strongest ascent, positive  $\theta_e$  anomalies, and vertical deformation of  $\theta_e$  isentropes. Moreover, the equatorward advection of positive  $\theta_e$  anomalies into the RRE domain resembles a weak gravity-current-like structure at its head. The resemblance of this structure is also evident in the negative anomalies of  $\theta$  at the lower levels and positive anomalies above.

When evaluating the MetUM forecasts, we find that there is an overall wet bias on the synoptic scale, while precipitation is underestimated over the RRE domain during the wet surges and particularly during the extreme rainfall days. The regional underestimation is attributable to the forecast error of convection initiation and organization. Despite these biases in the MetUM forecasts, there is overall good agreement with the reanalysis and GPM in the synoptic-scale patterns for both the spatial and temporal surge structure. The model forecast fields also appear to be continuous between the lead times of 33 and 12 hr in the temporal structure plots over the transect region, suggesting that the model forecasts perform well at these selected lead times on the synoptic scale. Spatially, the RRMSE is higher in the evaluation of the precipitation rate compared to the horizontal winds because of the mixture of wet and dry biases in the model forecasts. There is also a relatively low RRMSE in the transect comparison of  $B_L$  despite the overestimation over most of the transect region. Here, both the MetUM forecasts and ERA5 agree that the width of the convective region becomes narrower and restricted to the south of the equator when transitioning between the wet and dry surges. This is consistent with the narrowing and southward movement of the ITCZ (McBride et al., 2015; Xavier et al., 2020). Over the RRE domain, the MetUM forecasts overestimate both  $B_L$  and TCWV compared to the reanalysis, implying a generally moist bias and higher instability in the forecasts.

Overall, the convection-permitting model forecasts are of sufficient resolution to detail the response of convection to cold surges. Such mesoscale analysis cannot be performed on GPM since the horizontal grid spacing is too coarse. We conclude from our results that the model generally performs well synoptically but not in the details of mesoscale convection. One possible explanation for this caveat involves an issue with the standard cold-start technique of the model where the model is initialized directly from a global analysis, meaning that more time is required to generate convective structures and precipitation compared to the 12 km parameterized convection model (Lean et al., 2008; Warner et al., 2023). In other words, the early part of the forecast is unusable since there is a deficit of precipitation at the start of the forecast runs. A recommendation for future work would be to use convection-permitting forecasts that apply a warm-starting method. This method involves periodically inserting large-scale information from global model analyses into a continuously cycling regional model (Short & Petch, 2022; Warner et al., 2023). It improves the initialization of the forecasts by updating the large-scale information and preserving the fine-scale structures, thereby reducing the spin-up of precipitation significantly in the first 6–12 hr of the forecast compared to cold-starting. This is likely to improve the forecast rainfall skill and to address the wet and dry biases in the analysis of convection associated with cold surges.

Finally, we note that the wet biases may soon be addressed in the RAL3 package (refer to Table 1), which uses new microphysics and cloud schemes. This package is about halfway through its development at the present time. One of the main features of RAL3 is that it uses a single configuration in both the tropics and midlatitudes. Moreover, this new package should significantly improve the rainfall probability density function, with reduced peak rainfall rates while showing more widespread areas of light stratiform rain, thereby reducing the overall wet bias.

## Data Availability Statement

All data used in this manuscript are publicly available. The Met Office Managed Archive Storage System (MASS) was used to extract the MetUM forecast data sets for analysis as part of the JASMIN services (JASMIN, 2020). The ERA5 data sets are publicly available at Hersbach et al. (2023b) for single levels and Hersbach

## Acknowledgments

Tan was funded by the Monash International Tuition Scholarship (MITS) and the Maxwell King PhD Scholarship. Birch and Peatman were funded by the Natural Environmental Research Council (NERC) large grant, TerraMaris (NE/R016739/1); and by the FORcasting for SouthEast Asia (FORSEA) project, funded by the Met Office Weather and Climate Science for Service Partnership (WCSSP) Southeast Asia, as part of the Newton Fund. We are grateful for the use of JASMIN, the UK's data analysis facility for environmental science, to analyze the MetUM forecast data. We are also grateful to the National Computational Infrastructure (NCI) facilities to analyze ERA5 data that was originally downloaded from the Copernicus Climate Change Service (C3S) Climate Data Store, GPM-IMERG data from Goddard Earth Sciences Data and Information Services Centre and the Wheeler-Hendon MJO index from the Australian Bureau of Meteorology. Open access publishing facilitated by Monash University, as part of the Wiley - Monash University agreement via the Council of Australian University Librarians.

## References

- et al. (2023a) for pressure levels. The National Computational Infrastructure (NCI) supercomputer (NCI, 2021) was remotely accessed to analyze the ERA5 data sets from the rt52 workspace. The GPM data may be obtained from Huffman et al. (2023a) for daily data and Huffman et al. (2023b) for half-hourly data. Daily MJO data are available from the Australian Bureau of Meteorology (Bureau of Meteorology, 2023).
- Adames, Á. F., Powell, S. W., Ahmed, F., Mayta, V. C., & Neelin, J. D. (2021). Tropical precipitation evolution in a buoyancy-budget framework. *Journal of the Atmospheric Sciences*, 78(2), 509–528. <https://doi.org/10.1175/JAS-D-20-0074.1>
- Argüeso, D., Romero, R., & Homar, V. (2020). Precipitation features of the Maritime continent in parameterized and explicit convection models. *Journal of Climate*, 33(6), 2449–2466. <https://doi.org/10.1175/JCLI-D-19-0416.1>
- Bureau of Meteorology. (2023). Madden-Julian oscillation (MJO). [Dataset]. Australian Government Bureau of Meteorology. Retrieved from <http://www.bom.gov.au/climate/mjo/>
- Bush, M., Allen, T., Bain, C., Boulte, I., Edwards, J., Finnenkoetter, A., et al. (2020). The first Met Office unified model–JULES regional atmosphere and land configuration, RAL1. *Geoscientific Model Development*, 13(4), 1999–2029. <https://doi.org/10.5194/gmd-13-1999-2020>
- Bush, M., Boulte, I., Edwards, J., Finnenkoetter, A., Franklin, C., Hanley, K., et al. (2022). The second Met Office unified model/JULES regional atmosphere and land configuration, RAL2. *Geoscientific Model Development Discussions*, 2022, 1–35. <https://gmd.copernicus.org/preprints/gmd-2022-209/>
- Chang, C.-P., Erickson, J. E., & Lau, K. M. (1979). Northeasterly cold surges and near-equatorial disturbances over the winter MONEX area during December 1974. Part I: Synoptic aspects. *Monthly Weather Review*, 107(7), 812–829. [https://doi.org/10.1175/1520-0493\(1979\)107<812:NCSANE>2.0.CO;2](https://doi.org/10.1175/1520-0493(1979)107<812:NCSANE>2.0.CO;2)
- Chang, C.-P., Harr, P. A., & Chen, H.-J. (2005). Synoptic disturbances over the equatorial South China Sea and western Maritime continent during boreal winter. *Monthly Weather Review*, 133(3), 489–503. <https://doi.org/10.1175/MWR-2868.1>
- Chang, C.-P., Liu, C.-H., & Kuo, H.-C. (2003). Typhoon Vamei: An equatorial tropical cyclone formation. *Geophysical Research Letters*, 30(3). <https://doi.org/10.1029/2002GL016365>
- Chang, C.-P., Lu, M.-M., & Wang, S. (2004). The East Asian winter monsoon. In *The global monsoon system* (pp. 99–109).
- Chang, C.-P., Millard, J. E., & Chen, G. T. (1983). Gravitational character of cold surges during winter MONEX. *Monthly Weather Review*, 111(2), 293–307. [https://doi.org/10.1175/1520-0493\(1983\)111<293:GCOCSD>2.0.CO;2](https://doi.org/10.1175/1520-0493(1983)111<293:GCOCSD>2.0.CO;2)
- Clark, P., Roberts, N., Lean, H., Ballard, S. P., & Charlton-Perez, C. (2016). Convective-permitting models: A step-change in rainfall forecasting. *Meteorological Applications*, 23(2), 165–181. <https://doi.org/10.1002/met.1538>
- Davies, T., Cullen, M. J. P., Malcolm, A. J., Mawson, M. H., Staniforth, A., White, A. A., & Wood, N. (2005). A new dynamical core for the Met Office's global and regional modelling of the atmosphere. *Quarterly Journal of the Royal Meteorological Society*, 131(608), 1759–1782. <https://doi.org/10.1256/qj.04.101>
- Ding, Y. (1990). Build-up, air mass transformation and propagation of Siberian high and its relations to cold surge in East Asia. *Meteorology and Atmospheric Physics*, 44(1), 281–292. <https://doi.org/10.1007/BF01026822>
- Ding, Y. (1994). *Monsoons over China* (pp. 91–173). Kluwer Academic Publishers.
- Dipankar, A., Webster, S., Sun, X., Sanchez, C., North, R., Furtado, K., et al. (2020). Singv: A convective-scale weather forecast model for Singapore. *Quarterly Journal of the Royal Meteorological Society*, 146(733), 4131–4146. <https://doi.org/10.1002/qj.3895>
- Ferrett, S., Frame, T. H. A., Methven, J., Holloway, C. E., Webster, S., Stein, T. H. M., & Cafaro, C. (2021). Evaluating convection-permitting ensemble forecasts of precipitation over Southeast Asia. *Weather and Forecasting*, 36(4), 1199–1217. <https://doi.org/10.1175/waf-d-20-0216.1>
- Ferrett, S., Yang, G.-Y., Woolnough, S. J., Methven, J., Hodges, K., & Holloway, C. E. (2020). Linking extreme precipitation in Southeast Asia to equatorial waves. *Quarterly Journal of the Royal Meteorological Society*, 146(727), 665–684. <https://doi.org/10.1002/qj.3699>
- Fong, M., & Ng, L. K. (2012). *The weather and climate of Singapore* (pp. 70–97). Meteorological Service Singapore.
- Hai, O. S., Samah, A. A., Chenoli, S. N., Subramaniam, K., & Ahmad Mazuki, M. Y. (2017). Extreme rainstorms that caused devastating flooding across the East coast of Peninsular Malaysia during November and December 2014. *Weather and Forecasting*, 32(3), 849–872. <https://doi.org/10.1175/waf-d-16-0160.1>
- Hersbach, H., Bell, B., Berrisford, P., Biavati, G., Horányi, A., Muñoz-Sabater, J., et al. (2023a). ERA5 hourly data on pressure levels from 1940 to present [Dataset]. *Copernicus Climate Change Service (C3S) Climate Data Store (CDS)*. <https://cds.climate.copernicus.eu/cdsapp#!/dataset/reanalysis-era5-pressure-levels?tab=overview>
- Hersbach, H., Bell, B., Berrisford, P., Biavati, G., Horányi, A., Muñoz-Sabater, J., et al. (2023b). ERA5 hourly data on single levels from 1940 to present [Dataset]. *Copernicus Climate Change Service (C3S) Climate Data Store (CDS)*. <https://cds.climate.copernicus.eu/cdsapp#!/dataset/reanalysis-era5-single-levels?tab=overview>
- Hersbach, H., Bell, B., Berrisford, P., Hirahara, S., Horányi, A., Muñoz-Sabater, J., et al. (2020). The ERA5 global reanalysis. *Quarterly Journal of the Royal Meteorological Society*, 146(730), 1999–2049. <https://doi.org/10.1002/qj.3803>
- Hongming, Y., Yuan, Y., Guirong, T., & Yucheng, Z. (2022). Possible impact of sudden stratospheric warming on the intraseasonal reversal of the temperature over East Asia in winter 2020/21. *Atmospheric Research*, 268, 106016. <https://doi.org/10.1016/j.atmosres.2022.106016>
- Huffman, G. J., Bolvin, D. T., Braithwaite, D., Hsu, K., Joyce, R., Kidd, C., et al. (2019). NASA global precipitation measurement (GPM) integrated multi-satellite retrievals for GPM (IMERG). In *Algorithm theoretical basis document (ATBD) version 06*. National Aeronautics and Space Administration.
- Huffman, G. J., Stocker, E. F., Bolvin, D. T., Nelkin, E. J., & Tan, J. (2023a). GPM IMERG final precipitation L3 1 day 0.1 degree x 0.1 degree V07 [Dataset]. *Goddard Earth Sciences Data and Information Services Centre (GES DISC)*. [https://disc.gsfc.nasa.gov/datasets/GPM\\_3IMERGDF\\_07/summary](https://disc.gsfc.nasa.gov/datasets/GPM_3IMERGDF_07/summary)
- Huffman, G. J., Stocker, E. F., Bolvin, D. T., Nelkin, E. J., & Tan, J. (2023b). GPM IMERG final precipitation L3 half hourly 0.1 degree x 0.1 degree V07 [Dataset]. *Goddard Earth Sciences Data and Information Services Centre (GES DISC)*. [https://disc.gsfc.nasa.gov/datasets/GPM\\_3IMERGH\\_07/summary](https://disc.gsfc.nasa.gov/datasets/GPM_3IMERGH_07/summary)
- JASMIN. (2020). JASMIN [The UK's data analysis facility for environmental science]. Retrieved from <https://jasmin.ac.uk/>
- Johnson, R. H., & Chang, C.-P. (2007). Winter MONEX: A quarter-century and beyond. *Bulletin of the American Meteorological Society*, 88(3), 385–388. [www.jstor.org/stable/26217263](https://www.jstor.org/stable/26217263)
- Johnson, R. H., & Houze, R. A., Jr. (1987). Precipitating cloud systems of the Asian monsoon. *Monsoon Meteorology*. <https://ci.nii.ac.jp/naid/10014597164/en/>

- Kumar, A. (2021). A new approach to cold surge classification in East Asia. *Scientific Reports*, 11(1), 23659. <https://doi.org/10.1038/s41598-021-02873-0>
- Kumar, A., Lo, E., & Switzer, A. (2019). Relationship between east Asian cold surges and synoptic patterns: A new coupling framework. *Climate*, 7(2), 30. <https://doi.org/10.3390/cli7020030>
- Lau, K.-M., & Li, M.-T. (1984). The monsoon of East Asia and its global associations—A survey. *Bulletin of the American Meteorological Society*, 65(2), 114–125. [https://doi.org/10.1175/1520-0477\(1984\)065<0114:TMOEAA>2.0.CO;2](https://doi.org/10.1175/1520-0477(1984)065<0114:TMOEAA>2.0.CO;2)
- Lean, H. W., Clark, P. A., Dixon, M., Roberts, N. M., Fitch, A., Forbes, R., & Halliwell, C. (2008). Characteristics of high-resolution versions of the Met Office unified model for forecasting convection over the United Kingdom. *Monthly Weather Review*, 136(9), 3408–3424. <https://doi.org/10.1175/2008mwr2332.1>
- Lim, H., & Chang, C.-P. (1981). A theory for midlatitude forcing of tropical motions during winter monsoons. *Journal of the Atmospheric Sciences*, 38(11), 2377–2392. [https://doi.org/10.1175/1520-0469\(1981\)038<2377:ATFMFO>2.0.CO;2](https://doi.org/10.1175/1520-0469(1981)038<2377:ATFMFO>2.0.CO;2)
- Lim, S. Y., Marzin, C., Xavier, P., Chang, C.-P., & Timbal, B. (2017). Impacts of boreal winter monsoon cold surges and the interaction with MJO on Southeast Asia rainfall. *Journal of Climate*, 30(11), 4267–4281. <https://doi.org/10.1175/JCLI-D-16-0546.1>
- Ma, T., Chen, W., Gong, H., Hu, P., Jiao, Y., An, X., & Wang, L. (2022). Linkage of strong intraseasonal events of the East Asian winter monsoon to the tropical convections over the western pacific. *Remote Sensing*, 14(13), 2993. <https://doi.org/10.3390/rs14132993>
- Mapes, B. E., Chung, E. S., Hannah, W. M., Masunaga, H., Wimmers, A. J., & Velden, C. S. (2018). The Meandering Margin of the meteorological moist tropics. *Geophysical Research Letters*, 45(2), 1177–1184. <https://doi.org/10.1002/2017GL076440>
- McBride, J. I., Sahany, S., Hassim, M. E. E., Nguyen, C. M., Lim, S.-Y., Rahmat, R., & Cheong, W.-K. (2015). The 2014 record dry spell at Singapore: An intertropical convergence Zone (ITCZ) drought. *Bulletin of the American Meteorological Society*, 96(12), S126–S130. <https://doi.org/10.1175/bams-d-15-00117.1>
- Meteorological Service Singapore [MSS]. (2021). Warm weather with some short Thundery Showers in the next fortnight. Retrieved from <http://www.weather.gov.sg/fwo-warm-weather-with-some-short-thundery-showers-in-the-next-fortnight/>
- Meteorological Service Singapore [MSS]. (2022). 2021 annual climate assessment Singapore. Retrieved from <http://www.weather.gov.sg/climate-annual-climate-reports/>
- Meteorological Service Singapore [MSS]. (2023). *Weather systems*. Retrieved from [http://www.weather.gov/learn\\_weather\\_systems/](http://www.weather.gov/learn_weather_systems/)
- NCI. (2021). NCI Australia [ComputationalInfrastructure]. Retrieved from <https://nci.org.au/>
- Neale, R., & Slingo, J. (2003). The Maritime continent and its role in the global climate: A GCM study. *Journal of Climate*, 16(5), 834–848. [https://doi.org/10.1175/1520-0442\(2003\)016<0834:TMCAIR>2.0.CO;2](https://doi.org/10.1175/1520-0442(2003)016<0834:TMCAIR>2.0.CO;2)
- News.Az. (2021). Six dead, nearly 50,000 evacuated in Malaysia floods. Retrieved from <https://www.news.az/news/six-dead-nearly-50000-evacuated-in-malaysia-floods>
- OCHA Services. (2021). Malaysia: Floods – Jan 2021. Retrieved from <https://reliefweb.int/disaster/fl-2021-00001-mys>
- Pullen, J., Gordon, A. L., Flatau, M., Doyle, J. D., Villanoy, C., & Cabrera, O. (2015). Multiscale influences on extreme winter rainfall in the Philippines. *Journal of Geophysical Research: Atmospheres*, 120(8), 3292–3309. <https://doi.org/10.1002/2014JD022645>
- Ramage, C. S. (1971). *Monsoon Meteorology* (pp. 229–242). Academic Press.
- Senior, N. V., Matthews, A. J., Webber, B. G. M., Webster, S., Jones, R. W., Permana, D. S., et al. (2023). Extreme precipitation at Padang, Sumatra triggered by convectively coupled Kelvin waves. *Quarterly Journal of the Royal Meteorological Society*, 149(755), 2281–2300. <https://doi.org/10.1002/qj.4506>
- Short, C. J., & Petch, J. (2022). Reducing the spin-up of a regional NWP system without data assimilation. *Quarterly Journal of the Royal Meteorological Society*, 148(745), 1623–1643. <https://doi.org/10.1002/qj.4268>
- Smith, R. K., & Reeder, M. J. (1988). On the movement and low-level structure of cold fronts. *Monthly Weather Review*, 116(10), 1927–1944. [https://doi.org/10.1175/1520-0493\(1988\)116<1927:OTMALL>2.0.CO;2](https://doi.org/10.1175/1520-0493(1988)116<1927:OTMALL>2.0.CO;2)
- Tan, I., Reeder, M. J., Singh, M. S., Birch, C. E., & Peatman, S. C. (2023). Wet and dry cold surges over the Maritime continent. *Journal of Geophysical Research: Atmospheres*, 128(12), e2022JD038196. <https://doi.org/10.1029/2022JD038196>
- Tangang, F. T., Juneng, L., Salimon, E., Vinayachandran, P. N., Seng, Y. K., Reason, C. J. C., et al. (2008). On the roles of the northeast cold surge, the Borneo vortex, the Madden-Julian Oscillation, and the Indian Ocean Dipole during the extreme 2006/2007 flood in southern Peninsular Malaysia. *Geophysical Research Letters*, 35(14). <https://doi.org/10.1029/2008GL033429>
- Torgerson, W., Schwendike, J., Ross, A., & Short, C. J. (2023). Intensity fluctuations in Hurricane Irma (2017) during a period of rapid intensification. *Weather and Climate Dynamics*, 4(2), 331–359. <https://doi.org/10.5194/wcd-4-331-2023>
- van der Linden, R., Fink, A. H., Pinto, J. G., Phan-Van, T., & Kiladis, G. N. (2016). Modulation of daily rainfall in southern Vietnam by the Madden-Julian oscillation and convectively coupled equatorial waves. *Journal of Climate*, 29(16), 5801–5820. <https://doi.org/10.1175/jcli-d-15-0911.1>
- Warner, J. L., Petch, J., Short, C. J., & Bain, C. (2023). Assessing the impact of a NWP warm-start system on model spin-up over tropical Africa. *Quarterly Journal of the Royal Meteorological Society*, 149(751), 621–636. <https://doi.org/10.1002/qj.4429>
- Wheeler, M. C., & Hendon, H. H. (2004). An all-season real-time multivariate MJO index: Development of an index for monitoring and prediction. *Monthly Weather Review*, 132(8), 1917–1932. [https://doi.org/10.1175/1520-0493\(2004\)132<1917:aarmmi>2.0.co;2](https://doi.org/10.1175/1520-0493(2004)132<1917:aarmmi>2.0.co;2)
- Wu, P., Hara, M., Fudeyasu, H., Yamanaka, M. D., Matsumoto, J., Syamsudin, F., et al. (2007). The impact of trans-equatorial monsoon flow on the formation of repeated torrential rains over Java island. *SOLA*, 3, 93–96. <https://doi.org/10.2151/sola.2007-024>
- Xavier, P., Lim, S. Y., Ammar Bin Abdullah, M. F., Bala, M., Chenoli, S. N., Handayani, A. S., et al. (2020). Seasonal dependence of cold surges and their interaction with the Madden-Julian oscillation over Southeast Asia. *Journal of Climate*, 33(6), 2467–2482. <https://doi.org/10.1175/JCLI-D-19-0048.1>
- Xia, L., Zhang, J., & Hu, Y. (2024). Climatic interactions between cold surges in the South China Sea and North Pacific extratropical cyclones. *Meteorological Applications*, 31(2), e2182. <https://doi.org/10.1002/met.2182>
- Zerroukat, M., & Shipway, B. J. (2017). ZLF (zero lateral flux): A simple mass conservation method for semi-Lagrangian-based limited-area models. *Quarterly Journal of the Royal Meteorological Society*, 143(707), 2578–2584. <https://doi.org/10.1002/qj.3108>
- Zhang, Y., Si, D., Ding, Y., Jiang, D., Li, Q., & Wang, G. (2022). Influence of major stratospheric sudden warming on the unprecedented cold wave in East Asia in January 2021. *Advances in Atmospheric Sciences*, 39(4), 576–590. <https://doi.org/10.1007/s00376-022-1318-9>
- Zheng, F., Yuan, Y., Ding, Y., Li, K., Fang, X., Zhao, Y., et al. (2022). The 2020/21 extremely cold winter in China influenced by the synergistic effect of La Niña and warm Arctic. *Advances in Atmospheric Sciences*, 39(4), 546–552. <https://doi.org/10.1007/s00376-021-1033-y>